1290

UNIVERSIDADE Ð COIMBRA

Jéssica Lúcia Ferraz Carvalho

MECHANICAL DEVELOPMENT OF A MOBILE AUTONOMOUS ROBOT FOR MEDICAL APPLICATIONS

Outubro de 2021

Mechanical development of a mobile autonomous robot for medical applications

Submitted in Partial Fulfilment of the Requirements for the Degree of Master's in Mechanical Engineering in the speciality of Production and Project

Desenvolvimento mecânico de um robot móvel autónomo para aplicações médicas

Author

Jéssica Lúcia Ferraz Carvalho

Advisors

Professora Doutora Ana Paula Bettencourt Martins Amaro
Engenheiro António Santos

Jury

President	Professor Doutor Ricardo Nuno Madeira Soares Branco Professor Auxiliar da Universidade de Coimbra
Vowel	Professor Doutor Fernando Jorge Ventura Antunes Professor Auxiliar c/ Agregação da Universidade de Coimbra
Advisor	António Santos Active Space Technologies

Institutional Collaboration

Active Space Technologies, S.A.

Coimbra, October, 2021

ACKNOWLEDGEMENTS

Abstract

Automation has grown in the healthcare sector, mainly as a tool for autonomous disinfection, partly because of the rise of the COVID-19 pandemic. Active Space Technologies develops autonomous mobile robots for multiple applications, including disinfection. Therefore, the main objective of the work presented is the development of the chassis and associated mechanical structures of an Autonomous Mobile Robot (AMR) capable of operating in the healthcare sector, with limited dimensions and operational conditions adapted to the current pandemic situation.

In this project, all the relevant information concerning the technologies present in mobile robot systems were collected and an Autonomous Mobile Robot was designed. The AMR is planned with a differential drive, a traction/suspension system, electric components, and a lifting mechanism. All these components are supported and protected by the chassis and frame structure also devised. The structure is subjected to static, modal and fatigue assessments to evaluate its capacity to withstand the required loads and stresses.

After analysing the results of the structure assessment, it was possible to conclude that the AMR designed complies with all the requirements initially established. However, some work considering the UV resistant polymer and a practical fatigue test should be done.

Resumo

A automação tem vindo a crescer no setor da saúde, mais concretamente como uma ferramenta de desinfeção, em parte devido ao aumento da pandemia COVID-19. A Active Space Technologies desenvolve robôs móveis autónomos para várias aplicações, incluindo a desinfeção. Portanto, o objetivo primário do trabalho apresentado é o desenvolvimento do chassis e estruturas mecânicas associadas de um Robô Móvel Autónomo (RMA) capaz de operar no setor da saúde, capaz de operar no setor de saúde, com dimensões e condições de operação limitadas adaptadas à atual situação pandémica.

Neste projeto, foram recolhidas todas as informações relativas às tecnologias presentes nos sistemas dos robôs móveis e foi concebido um Robô Móvel Autónomo. O RMA está planeado com uma transmissão diferencial, um sistema de suspensão/tração, componentes elétricos, e um sistema de elevação. Todos estes componentes estão suportados e protegidos pelo chassis e estrutura também projetados. A estrutura é sujeita a análises estáticas, modais e de fadiga para avaliar a sua capacidade de suportar as cargas e tensões requeridas.

Depois de analisar os resultados das análises da estrutura, foi possível concluir que o RMA projetado cumpre todos os requisitos inicialmente estabelecidos. Contudo, alguns estudos considerando o polímero resistente aos raios UV e um teste prático à fadiga devem ser realizados.

Palavras-chave: AMR / MRA, Transmissão diferencial, Desenho, Análise de Elementos finitos, Suspensão por mola, Robô.

CONTENTS

LIST OF FIGURES

LIST OF TABLES

LIST OF SIMBOLS AND ACRONYMS/ ABBREVIATIONS

List of Symbols

a, b – Distance between the centre of the bearing and the pressure point

a – Acceleration

a_1 – Life adjustment factor

a_{SKF} – SKF life modification factor

A – Autonomy

B – Battery capacity

$\mathbf{B}(\boldsymbol{q})$ – Input matrix

B_{Total} – Total battery capacity

C – Basic dynamic load

C_0 – Static basic load

$C_1, \dots, C_5$ – Coefficients related to the kinematic constraints

d – Distance between the centre of mass and the mid-point

e, Y – Calculation factor

E – Net mass of the transport equipment

$\mathrm{E_c}$ – Kinetic energy

$\mathrm{E_p}$ – Potential energy

$\mathbf{F}$ – Generalized force vector

$\mathrm{F_a}$ – Friction force

F_{max} – Maximum load

F_{med} – Mean load

F_{min} – Minimum load

$\mathrm{F_r}$ – Radial Load

$\mathrm{F_{R_{Ly}}}, \mathrm{F_{R_{Ry}}}, \mathrm{F_{R_{Lx}}}, \mathrm{F_{R_{Rx}}}$ – Bearing reaction forces

$\mathrm{F_s}$ – Actuator force

g – Gravitational acceleration

i – Gearbox ratio

I – Electric current

I_c – Moment of inertia about the vertical axis through the centre of mass

I_m – Moment of inertia of each traction wheel (with DC motor) about the wheel diameter

I_w – Moment of inertia of each traction wheel (with DC motor) about the wheel axis

I_z – Moment of inertia of rotating masses

K_A – External axial force

L – Distance between the traction wheels and the symmetry axis of the robot

L, H – Distance between the bearing and the wheel

L_{nmh} – SKF rating life

m – Mass of the AMR

m_c – Mass of the AMR without the driving wheels

m_{eq} – Equivalent mass

m_q – Mass of one-quarter of the load

m_w – Mass of each driving wheel (with DC motors)

$\mathbf{M}(\boldsymbol{q})$ – Generalized coordinates matrix

M_m – Moment of the motor

M_R – Moment of the wheel

n – Number of supporting wheels or castors

n_b – Number of batteries

n – failure probability

n_m – Angular velocity of the motor

N – Radial force

p – exponent of the life equation

P – Equivalent dynamic bearing load

P – Power

P_0 – Equivalent static load

P_{sm} – Power of one motor

$\boldsymbol{q^g}, \boldsymbol{q}, \boldsymbol{q_i}$ – Coordinates vector

Q – Reamining charge

r – Wheel radius

S – Safety factor

S_0 – Static safety factor

$S_1, ..., S_n$ – Spring compression rating

$\mathbf{S}(\mathbf{q})$ – Transformation matrix

t – Time

T – Torque

T_D – Dynamic load capacity

ν – Actual operating viscosity

ν_1 – Rated viscosity

v – linear velocity

V – Voltage

$\mathbf{V}(\mathbf{q}, \dot{\mathbf{q}})$ – Coriolis and centrifugal matrix

ω – Angular velocity

ω_m – Angular velocity of the motor

ω_r – Angular velocity of the wheels

W_{ext} – External work

W_{int} – Internal work

x_1 – Height of the lever

x_2 – Length of the lever

x_a, y_a – Coordinates of the geometric centre of the robot

x_c, y_c – Coordinates of the centre of mass of the robot

X_g, Y_g – Global reference frame axis

X_R, Y_R – Local reference frame axis

Z – Load

$\boldsymbol{\eta}$ – Angular velocity of the wheels vector

η_c – Level of contamination

f – Frequency

$\dot{\varphi}_L, \dot{\varphi}_R$ – Angular velocity of left and right taction wheels

κ – Lubrification condition

$\boldsymbol{\lambda}$– Lagrange multiplier vector

$\mathbf{\Lambda}(\boldsymbol{q})$ – Constraints matrix

μ_c – Rolling resistance coefficient

μ_e – Static coefficient of friction

μ_{gb} – Efficiency of the gearbox

$\boldsymbol{\tau}$ – input vector

θ – Angle between the global and local reference frame

Acronyms/Abbreviations

ABS – Acrylonitrile Butadiene Styrene

AC – Alternative Current

AGV – Autonomous Guided Vehicle

AMR – Autonomous Mobile Robot

AST – Active Space Technologies

ASTM – American Society for Testing and Materials

BLDC – Brushless DC

CAD – Computer Aided Design

COVID-19 – Coronavirus disease 2019

DC – Direct Current

DWB – Double Wishbone

FDA – Food and Drug Administration

FEA – Finite Element Analysis

GUV – Germicidal Ultraviolet

LED – Light-Emitting Diode

PFHd – Probability of a Dangerous Failure per Hour

PL – Performance Level

PLC – Programmable Logic Controller

PLr – Required Performance Level

SIL – Safety Integrity Level

SLAM – Simultaneous Localization And Mapping

STO – Safe Torque Off

SS1 – Safety Stop 1

SSI – Synchronous Serial Interface

SUV – Sport Utility Vehicle

UV – Ultraviolet

1. INTRODUCTION

Technological advancements and research have contributed to the expansion of tasks that can be executed by robots. Over the years robots have been replacing humans in many fields, namely planetary exploration, patrolling, industrial automation, personal services, intervention in extreme environments, transportation, and medical care (Rubio et al., 2019)

Mobile robots can move about a given space (factory floor, planetary surface, laboratory, etc.) without human aid. They are equipped with a system that collects data from their environment, analyses it and decides accordingly. Wheeled mobile robots such as Autonomous Guided Vehicles (AGV) are a rising force in logistics and distribution (Rubio et al., 2019).

Ever since their introduction in the 1950s, AGV navigation systems have evolved along mechanical, optical, inductive, cartesian, inertial and laser guidance into the most recent vision-based guidance or natural feature navigation. This latest system is comprised of ubiquitous sensors, onboard computers, artificial intelligence and Simultaneous Localization And Mapping (SLAM) technology (Fragapane et al., 2021). SLAM technology enables the robot to model the environment in which it moves through and estimates its position and orientation, simultaneously (Cebollada et al., 2021). These types of robots are called Autonomous Mobile Robots (AMR).

The AMR concept is not new. It was first patented in 1987 and has recently emerged in logistics applications. There are already examples of this technology: the *Omron LD Mobile Robot*, able to handle material in challenging environments (Omron[®], 2021); the *MiR500*, able to transport payloads of up to 500 kg at high speed (Mobile Industrial Robots A/S[®], 2020); and the *ADIBOT-A*, capable of disinfecting environments autonomously (UBTECH[®], 2020).

AMRs are a more flexible option for this project since they can move freely within a given area and can adapt quickly to changes in their environment. Furthermore, they can communicate and interact independently with other resources (i.e., machines and systems) and make decisions by themselves. In this way, each vehicle is able to optimize

itself and react more dynamically to changes or demands (Fragapane et al., 2021). Finally, they are easier to install because they do not require external guidance tools like magnetic strips or buried inductive wires.

All these strengths are well demonstrated in narrow and crowded spaces like warehouses and hospitals. AGVs do not enter these types of environments for safety and performance reasons. Meanwhile, AMRs can deliver critical or just-in-time goods, or can provide services such as disinfection or provide assistance. In conclusion, these robots effectively reduce material handling in hospitals, providing more time for patient-related activities (Fragapane et al., 2021)

1.1. Context and Motivation

The motivation for this dissertation emerged from one of the projects in development at Active Space Technologies (AST). AST is developing a modular AMR capable of disinfecting surfaces in hospitals and other buildings. During my internship, I followed this process while designing my own robot and considering all the necessary requirements. This meant that by the end of this work, AST would have two prototypes to compare and would be able to make a more informed decision.

AST is a European based company that operates in space, nuclear, industry and aeronautics. Founded in 2004, the company's work focuses on space instrumentation, structural and thermal control systems for space applications, harsh environments, monitoring and control systems for aerospace applications, remote handling systems for hazardous and radiation environments and automated systems for industry.

The company's subsidiary, Active Space Automation, offers highly flexible and efficient solutions for transporting materials and goods in manufacturing and storage facilities. It is a leader in the deployment of automated guided vehicles and robotics for a broad range of applications. For example, the *ActiveONE* product, capable of handling up to 800 kg and guided either with magnetic tape or natural navigation, is being used to transport parts around the Volkswagen car assembly plant in Palmela, Portugal.

Since late 2019, the COVID-19 disease has spread globally causing a pandemic. It brought serious challenges to almost every country on the planet. Up until September 2021, there have been more than 228 million confirmed COVID-19 cases with at least 4 million deaths globally, according to statistics from the World Health Organisation (2021).

It is a very contagious disease that puts the close contacts of an infected person in danger, even medical personnel. Robots are easily disinfected and have been suggested for various applications such as disinfection, monitoring, delivering, food preparation and telepresence (Wang and Wang, 2021).

As referred before, this dissertation focuses on mobility technology, more specifically in the development of a more compact and flexible design.

1.2. Objectives

The main objective of this work is to develop a modular mobile robot capable of disinfecting rooms with a UV light tower in hospitals and other buildings. This mobile robot shall be lightweight, fully autonomous, and capable of performing other tasks such as transportation of goods.

The chassis and associated mechanical structures, namely the motion and traction units, of the mobile robot are designed. The designed concepts are then static and dynamically analysed. Moreover, a kinematic and dynamic model of the AMR is developed.

1.3. Overview of the Dissertation

This dissertation is divided into five chapters. In Chapter 1 an introduction, motivation and objectives of the dissertation are given. In Chapter 2 it is presented a theorical background on the relevant technologies used to design the AMR. In Chapter 3 the design and development of the AMR is introduced. In Chapter 4 the model is validated statically and dynamically using Finite Element Analysis (FEA). Chapter 5 relates to the conclusions and suggestions for future projects.

2. STATE OF THE ART

In this chapter, a theoretical background concerning the components of an AGV is presented. According with the literature review of each component, the most common and recent technologies are summarized.

This chapter is divided into four sections: structure, locomotion mechanism, battery and charging, and navigation system. In the first one, examples of structures from previous work are given, along with types of loading systems. The following sections include the review of the kinds of driving configurations and their respective wheels, suspension systems already on the market and analysis of the various motors and gearboxes used for this application. In the third section, the charging system is explained, while the fourth and last section provides the assessment of different navigation technologies employed in AGVs.

2.1. Structure

The structure of any AGV must be made to accommodate all the main components: suspension, traction, load, navigation, and safety systems. It is built out of a material that can withstand the weight of the vehicle and the loading, but it is also lightweight and cost-effective.

To understand how structures are designed with the appropriate materials, some publications give their contributions (Archila and Becker, 2013; Dudeja et al., 2015; Razak et al., 2016). Frames comprised of rectangular ASTM 500 steel can be used to reduce more bulky and heavy structures without compromising the ability to carry loads (Razak et al., 2016). Structural steel is also lightweight and rigid. Therefore, L beams of this material were used to build the structure (e. g., Archila and Becker, 2013). Figure 2.1A shows the CAD model of the structure developed and the final model of the AGV developed by Archila and Becker (2013). Another material used in frame manufacturing is Dent Proof Sheet Metal MS®. This material is easy to fabricate and reduces the overall weight of the vehicle (Dudeja et al., 2015). This particular structure, shown in Figure 2.1B, is designed to withstand a load of 800 kg. The frame is comprised of two MS C-channel hollow bars connected by three support plates also made of MS material. To distribute the weight in the vehicle, six mild steel boxes are situated between each C cross-section bar and support plates. All these

structures are welded together. Bolted joints can be used if the frame needs to be modular and able to disassemble without destroying any components (Carnegie et al., 2004).
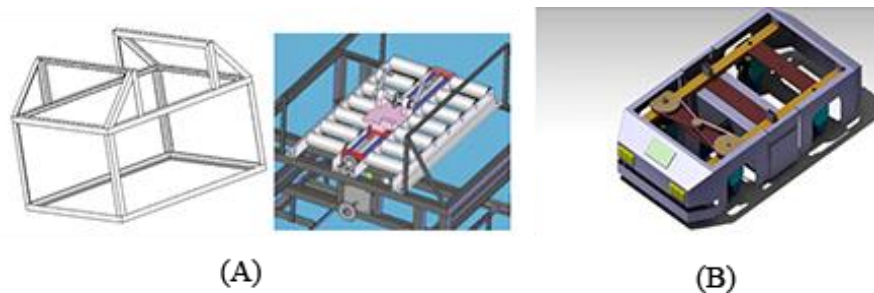
Figure 2.1. Structure and loading system of a structural steel frame (A); frame built of Dent Proof Sheet Metal MS (B) (Archila and Becker, 2013; Dudeja et al., 2015).

One of these components is the load system. There are various types suited for tasks the AGV is going to perform. When needed to move cargo from one place to another, the vehicle can be equipped with a pin hook, a conveyer, or an elevation platform. These systems are characteristic of a mouse AGV because the loading/unloading is done with the AGV positioned directly below the cargo (Patricio and Mendes, 2020).

ActiveONE, one of the AGVs developed by Active Space Technologies, has three standard versions: pin hook for towing (Figure 2.2A), hydraulic version with an elevation platform to lift and carry loads (Figure 2.2B) and a conveyor platform (Figure 2.2C) that can substitute pallet trucks.

(A)   (B)   (C)
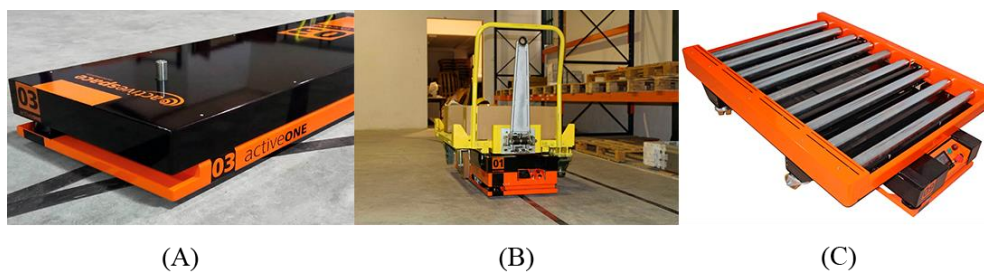
Figure 2.2. *ActiveONE* Pin Hook (A), *ActiveONE* Hydraulic (B), *ActiveONE* Conveyor (C) (Active Space Technologies, 2020).

2.2. Locomotion Mechanism

The locomotion mechanism used in the present work is defined by the wheels, motors, and respective gearboxes. Since mobile robots are designed to be autonomous, precise, and compact, electric motors are preferable over other technologies.

Wheeled robots require one or more driven wheels, optional caster wheels and steered wheels. The driving configuration designed determines the number and types of

wheels needed. Five designs are being used currently in mobile robots: single-wheel drive, differential drive, synchro-drive, Ackerman steering and omnidirectional drive.

The single-wheel drive is the simplest conceptual design by having just a single wheel for driving and steering. As three contact points are required to maintain stability, two additional castor wheels are necessary, as shown in Figure 2.3. Two motors have to be used in this design: one to drive and another to steer, which allows for separate turning and driving, simplifying the control software. However, because the drive wheel is not located in the centre, it cannot turn on the spot.
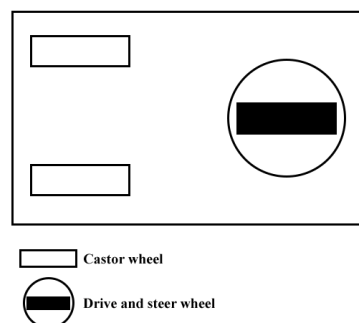
Figure 2.3. Single-Wheel drive.

Differential drive is the most common configuration in mobile robots. The driven wheels, each equipped with a motor, are mounted on either side of the robot, and driven independently from each other. To assure the three contact points, this design is fitted with at least one castor wheel. Figure 2.4 shows the differences between fitting one castor wheel and two. If only one castor wheel is fitted, the driven wheels are to be located on one end of the robot for stability. Moreover, similar to the single-wheel drive, this concept cannot turn on the spot. This last issue can be resolved by adding another caster wheel, allowing for the driven wheels to be moved to the centre of the robot (Tzafestas, 2014a).
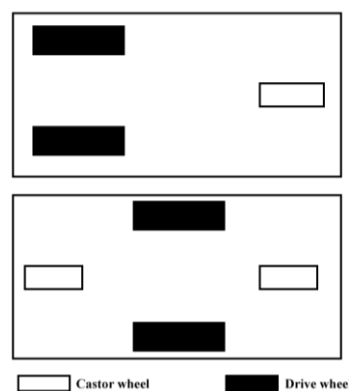
Figure 2.4. Differential drive.

The Ackermann Steering is typical in automobiles as it combines two driver wheels (rear) and two steering wheels (front). This allows for the separation of linear and angular velocity since one is generated in the rear engine and the latter is generated in the front engine. This, in turn, improves and facilitates control, especially when driving straight. This independent driving/steering mechanism can drive straight without any issues because the back wheels are driven on a common axis, as seen in Figure 2.5. Because of the specific wheel configuration, this concept does not allow the system to turn on the spot, but it requires a minimal radius (Bräunl, 2003).
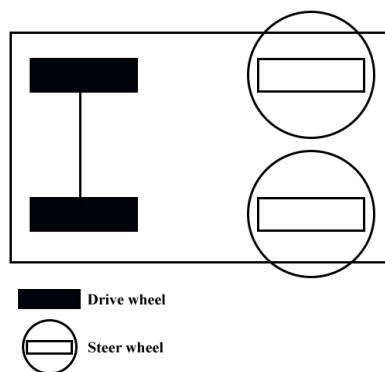
Figure 2.5. Ackermann Steering.

The omnidirectional drive design comprises three or four mecanum wheels. These wheels were patented by Bengt Ilon, an engineer in the Swedish company Mecanum AB®, in 1973 (Taipalus, 2004) and there are different wheel variants. Each wheel surface is fitted with a certain number of free rolling cylinders. Only the wheel hub is powered by the motor while the cylinders are held in place by ball-bearings. The rollers can be set at a 45° or 90° angle to the wheel axis; some examples are given in Figure 2.6. If the rollers are at a 45° angle to the wheel axis, the wheel becomes asymmetric (Bräunl, 2003).

Figure 2.6. Mecanum Wheels with rollers at 90^0 (left) and 45^0 (right) angle (OZ ROBOTICS®, 2021a, 2021b).

Looking at one individual wheel, the force generated at the roller that acts on the ground can be split in a vector longitudinal to the roller axis (Force A in Figure 2.7) and a vector perpendicular to the roller axis (Force B in Figure 2.7). Force A applies a force on the

wheel and therefore in the vehicle, and Force B delivers a small rotation to the roller (Bräunl, 2003).
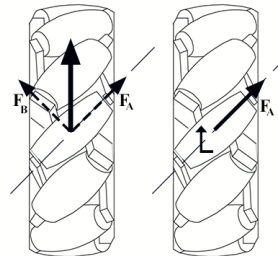
Figure 2.7. Force representation of the left-hand wheel. In this case, Force A represents the traction force.

When the wheels are assembled in a four-wheel assembly, vehicle motion is determined by the resulting wheel forces. So, forces A and B act as forward and sideway forces: the former adds up while the latter cancels each other out. To move the vehicle in various directions, the wheels must vary their rotation. Figure 2.8 shows the different configurations of the wheels to drive the vehicle backwards, forwards, left and right (Bräunl, 2003).
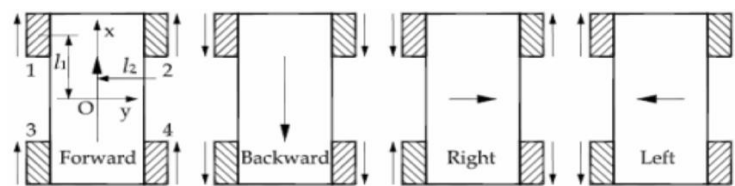
Figure 2.8. Mecanum principle, driving forward, backward and sliding right and left (Soni et al., 2014).

All these motions are obtained if the wheels are rotating at the same velocity. However, if one varies the speed magnitude of the wheels any motion in the 2-D plane can be accomplished.

2.2.1.   Suspension

For AMRs, the suspension serves two purposes: absorb vibrations and maintain the wheels on the ground despite terrain unevenness. Just like the structure, the suspension is fitted to the type of AMR and floor conditions. However, AMRs usually operate on relatively smooth surfaces and so they are not equipped with any suspension system. Therefore, there is not a lot of information available.

Premi (1985) developed an AGV with spring-loaded castor wheels that provided the suspension. This allows for each castor spring to be individually tensioned to give a variable suspension.

Dzezhyts (2020) designed a joint, so the weight is distributed between the two wheels. Springs are attached between the chassis and the base, as shown in Figure 2.9. This type of suspension is efficient in linear movement as long as the floor surface does not vary beyond twenty millimetres.

Figure 2.9. Complete suspension unit (Dzezhyts, 2020)**.**

Archila and Becker (2013) proposed a suspension system shown in Figure 2.10. It looks similar to a bicycle suspension with four shock absorbers bolted to the frame.
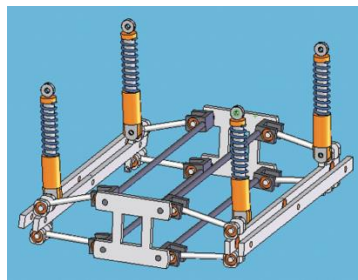
Figure 2.10. Suspension system developed by Archila and Becker (2013).

2.2.2. Motor and gearbox

Electric motors for AGV driving systems can be DC or AC powered motors and stepper motors.

Brushed and brushless motors are the most common DC motors. They have similar static characteristics, but they differ in some important aspects such as commutation. Commutation is the process that converts alternating current generated in the armature windings into direct current. In brushed motors, this process is done by a commutator and brushes, whereas in the brushless motor it is done by using semiconductor devices such as transistors (Gambhir and Jha, 2013).

Furthermore, brushed DC motors are characterised by their ability to achieve high torque at low speed, which is adequate for traction applications. Depending on power output and voltage requirements, these motors have between two and six poles. They are easily controllable, and their speed can be varied by adjusting the voltage. On the other hand,

they are bulky, less efficient but reliable. Also, because of its brushes and commutator, a higher need for maintenance is required and they cause higher levels of noise than brushless DC motors. Furthermore, it is difficult to downsize brushed DC motors making them more expensive and heavier.

Brushless DC motors (BLDC) use permanent magnets to generate the rotor's magnetic field. This motor is usually lighter and more compact, more powerful, has more speed ranges, requires less maintenance (because of the absence of brushes), and offers higher dynamic responses than brushed DC motors. Nevertheless, BLDC are more expensive, more complex (requiring more sophisticated control) and need additional system wiring to power the electronic commutation system (Gambhir and Jha, 2013; Xue et al., 2008).

Squirrel-cage induction motors are a type of AC motor. They are simple, reliable, low cost, and robust. They do not require permanent magnets or powered rotors. The rotor field is induced by the stator. This allows for the motor to have a higher speed rating, offering superior output. Speed can vary by controlling the power signal frequency applied to the stator and it is dependent on the number of poles. However, controllers for these motors are more expensive than those needed for DC motors. Induction motors have breakdown torque that limits their extended constant-power consumption. On a last note, these types of AC motors have a lower efficiency than BLDC motors since they do not have rotor windings (Xue et al., 2008).

Lastly, to drive an AMR successfully and safely, the electric motors need to be coupled to a transmission, brake system, and an optical or magnetic encoder. The latter assures the feedback mechanism needed to control the motor and therefore the AMR. A magnetic encoder consists of a disk fitted with magnets and one or two Hall-effect sensors. An optical encoder, in turn, comprises a disk with black and white sectors, an LED, and a reflection or transmission light sensor. If two sensors are positioned with a phase shift, one knows which one is triggered first. Thus, one can determine whether the motor shaft is being turned clockwise or counter clockwise.

2.3. Battery and charging

Since mobile robots use electric motors, a rechargeable battery pack is needed to power the engine. Selecting the right battery pack depends on various parameters such as size, capacity, power rating, discharge cycle, and cost.

The most common technologies are lead-acid batteries and nickel-cadmium batteries, though more recent technologies such as lithium-ion batteries have gained traction in this field (Ullrich, 2015).

Lead-acid (Pb-acid) batteries are the most common battery in AGVs (Martínez, 2020). It is a well-studied, robust, and reliable technology. Pb-acid batteries have a low internal impedance that allows for high currents, plus they can come in several sizes and voltage levels. Nevertheless, these batteries are usually heavy and bulky as lead is a heavy metal. Finally, they have long charging times that require the AMR to charge overnight or change its batteries (Ullrich, 2015).

Nickel-cadmium (Ni-Cd) batteries are more expensive than the previous ones but offer a longer service life and a bigger power density. They can be used in interval operations since the batteries are charged intermittently and do not need to be removed from the robot during the workday (Ullrich, 2015).

Lithium-ion (Li-ion) batteries are the lightest of the three and have the biggest energy density, higher capacity, and cycle life (number of complete discharge and charge cycles the battery can perform before its capacity is lower than 80 % of the initial rated capacity). Moreover, the environmental impact of this technology is significantly lower (Meena and Thilagavathi, 2012).

In order to make a more informed comparison of these three types of batteries, their properties are summarized in Table 2.1.

Table 2.1. Batteries Properties (Martínez, 2020)

	Pb-acid	**Ni-Cd**	**Li-ion**
Energy density (Wh L^{-1})	60-110	70-90	250-290
Specific Power (W kg^{-1})	285	220	Up to 1350

Cell Voltage (V)	2.1	1.2	3.7
Capacity (mAh)	4000-7000	600	2000-6000
Number of Charges	700	1500	500-2000
Theoretical Life Time (years)	3	2	6
Recharge Time (h)	8	1	2-3
Memory Effect	No	Yes	No
Maintenance	No	Yes	No

The charging method and associated management scheme are also very important since they define how much time the robot is offline during a working day. Currently, there are four charging schemes (manual battery swap, automatic battery swap, opportunity charge and automatic charge).

Manual battery swap and automatic battery swap are very similar. The only difference lies in who replaces the battery. When it falls below a pre-defined value, the AMR goes to the charging station and an operator (manual swap), or a machine (automatic swap) removes the battery and replaces it with a fully charged one.

Opportunity charge uses the AMR idle time in the cycle to charge itself. This scheme is mostly used when the working cycle has many predictable and regular stops (for example in assembly systems). Since they are regularly charged, batteries are usually smaller. Moreover, no additional operation time is added because charging occurs when the AMR is stopped.

In automatic charging, the AMR will run until its battery reaches a certain level. Then, a central control system assigns a charging station to that vehicle and the battery is recharged until a predefined value. As the name implies, the charging process is done automatically. Additional time to replenish the batteries needs to be added so it may increase the number of robots needed in the system (McHaney, 1995).

2.4. Navigation System

Currently, there are five main forms of navigation for AMRs: laser, line-following, magnetic spot, barcode guidance, and natural feature navigation. They employ several types of sensors like laser scanners, optical and magnetic sensors.

Laser guidance uses a class 1 rotating laser positioned in the AMR to navigate. Reflective tape is placed within the area of operation to facilitate position location. The area of operation is also stored in the vehicle's onboard computer. It is very easy to install and expand, highly flexible and efficient and can deviate from its route. However, it is more costly and more complex than line following guidance or magnetic spot guidance.

In line following guidance, the AMR follows a pre-defined track path laid down on the area of operation. The track path can be made of magnetic tape or wire embedded in the floor. The vehicle has onboard sensors that detect the magnetic tape or wiring making it follow the desired path to the destination. It is a simple low cost and easy to install option. However, it is not very flexible, cannot deviate from routes, is harder to expand and is the least efficient technology out of the five.

Magnetic spot guidance is somewhat similar to line following guidance. It uses sensors beneath the AMR to detect the magnetic spots laid on the floor. The main difference is that this method does not need pre-defined tracks; instead, it can move through the operation area using reference points stored in the vehicle's memory. It is cheap and easy to install and can also deviate from routes. It is easily expandable, flexible, and efficient (but not as much as in laser guidance).

Barcode guidance is based on the same concept as magnetic spot guidance. The difference lies in using QR codes (or AprilTag technology) on the floor or walls in the working area that are detected by the AMR through a laser scanner or camera. This guidance system does not allow for deviations from routes despite being as flexible and efficient as the previous one (Lynch et al., 2018).

Natural feature navigation or contour navigation is the most recent technology. It uses a line scanners or cameras to gather data on the characteristics of the environment and SLAM (Simultaneous Localization And Mapping) technology to build a geometric map of the operating area. The AMRs route can be planned on the map. In the beginning, the vehicle will locate itself based on the map created and the current landmarks. The vehicle is also sensitive to a dynamic environment and can easily update the map as changes occur

(Chen et al., 2017). Therefore, this system is highly flexible and very easy to install. Moreover, there is no need to install other tools such as reflectors or magnetic tapes; the cost of installation is lower than the other methods of navigation (Association for Advancing Automation, 2021).

When discussing AMRs or other moving vehicles, one must ensure the safety of people and of the vehicle itself. This is done by the operation of sensors that detect obstacles and incoming dangers in the AMR path. The onboard computer is responsible for operating said sensors and controlling other relevant components such as motors, brakes, encoders, signal lights and emergency buttons. The most common tool for this is a Programmable Logic Controller (PLC). The PLC is programmed to perform a desired task and it is highly used in automation applications (Hubinský et al., 2013). This is capable of processing perceptions of environments very rapidly and can integrate several systems (for example, when connected to vision systems, the PLC is capable of detecting an obstacle and execute a command to avoid collision).

3. DESIGN AND DEVELOPMENT

Before selecting any components or systems some requirements have to be established to assure the design is fit for the application and follows crucial standards. AST has developed AMRs to allow for maximum flexibility of materials transportation in a warehouse or factory floor. Since it is not the first time AST is developing mobile robots, the following set of basic requirements is established:

1. Needs to comply with the regulations regarding equipment for the health sector.
2. It has to be capable of moving in tight spaces as well as rotating 360°.
3. It needs to be able to be immediately stopped in emergency cases.
4. Components that perform safety functions should have a performance level rating of PL d or better.
5. All the electronic parts must run on 24 V.
6. The maximum velocity falls between 1 and 1.5 m s^{-1}.
7. It should have a maximum mass of 100 kg and be able to withstand a load of at least 100 kg.
8. Width under 70 cm.
9. It will move around using natural feature navigation.
10. The AMR is powered by lithium-ion batteries and charged via wireless systems.

All the materials and components, in contact with the exterior, have to be compatible with UVC, ultraviolet light with wavelengths from 250 to 300nm, disinfection. As reported by the FDA (2021), UVC radiation has been effectively used to reduce the spread of bacteria, such as tuberculosis. Moreover, UVC lights have been proven to be effective at de-activating the SARS-CoV-2 virus, responsible for COVID-19 when put in direct contact at the right dose.

The vehicle shall be autonomous and able to move seamlessly through the environment. Hospitals have more narrow hallways and doors than factory floors. They are also more densely populated, and obstacles tend to change positions very frequently. For

these reasons, the robot has to be smaller than 70 cm wide so it can move around without any trouble.

Natural feature navigation is also a requirement since hospitals do not have the flexibility to install navigation equipment (i.e., magnetic tape or bar codes) along with constant floor layout changes.

In past years, AST has used batteries other than lithium-ion such as lead-acid batteries. AST has found that these batteries had less autonomy and were less reliable because their capacity tends to decrease over time. For these reasons, the company relies on lithium-ion batteries to power its AMRs.

In this chapter the kinematic and dynamic analysis is presented in the first section. In the following sections, the step-by-step assessment of components is done. The evaluation of the structure and frame of the AMR is presented in Section 3.5.

3.1. Kinematics and dynamics

The kinematic model is made assuming that the robot is a rigid body on wheels operating on a horizontal plane (Parhi and Deepak, 2011). To specify the position of the robot, a relationship between the robot reference frame $\{X_R, Y_R\}$ and the global reference frame $\{X_g, Y_g\}$ is established, as shown in Figure 3.1. The local reference frame $\{X_R, Y_R\}$ is positioned on the wheel's axis in the mid-point (A in Figure 3.1). The centre of mass is established by point C $\{x_c, y_c\}$. The angular difference between the robot and global frames is given by θ and the distance between the centre of mass and the mid-point A is d.
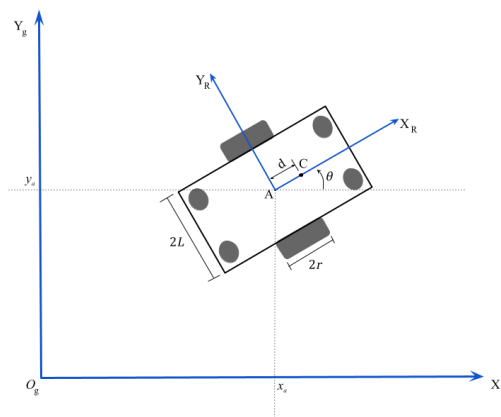
Figure 3.1. Robot definition in global reference frame.

The robot's position and orientation in the global reference frame is defined by

$$\boldsymbol{q^g} = [x_a \quad y_a \quad \theta]^T. \tag{3.1}$$

where

$$\begin{cases} x_c = x_a + d \cos \theta \\ y_c = y_a + d \sin \theta \end{cases}, \tag{3.2}$$

When the robot is in motion, it is typically assumed the pure rolling without slipping condition. This means the contact between the wheel and the ground can be reduced to a single point on the plane, as shown in Figure 3.2.
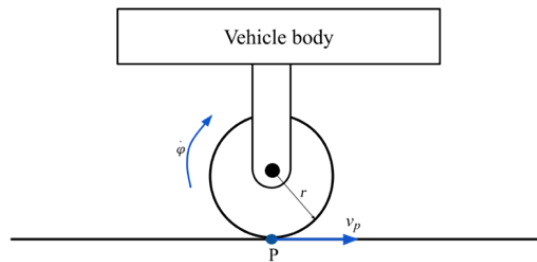
Figure 3.2. Wheel and rolling motion constraints representation.

The castor wheels of the robot are passive wheels, which means they do not add any constraints to the model. Therefore, the non-holonomic constraint under the no-slip condition is

$$-x_a \sin \theta + y_a \cos \theta = 0 \tag{3.3}$$

and under the pure rolling condition the non-holonomic constraints are

$$\begin{cases} \dot{x}_{pR} \cos \theta + \dot{y}_{pR} \sin \theta = r \, \dot{\varphi}_R \\ \dot{x}_{pL} \cos \theta + \dot{y}_{pL} \sin \theta = r \, \dot{\varphi}_L \end{cases}, \tag{3.4}$$

$$\begin{cases} \dot{x}_{pR} = \dot{x}_{pL} = \dot{x}_a + L \, \dot{\theta} \cos \theta \\ \dot{y}_{pR} = \dot{y}_{pR} = \dot{y}_a + L \, \dot{\theta} \sin \theta \end{cases} \tag{3.5}$$

where $\dot{\varphi}_R$ and $\dot{\varphi}_L$ are the angular velocities of the right and left wheels, respectively, r is the radius of the wheel, and L is the distance between the traction wheels and the symmetry axis of the vehicle (Dhaouadi and Hatab, 2013).

When combining Equations (3.3) and (3.5) we obtain:

$$\begin{cases} \dot{x}_a \cos \theta + \dot{y}_a \sin \theta + L \, \dot{\theta} - r \, \dot{\varphi}_R = 0 \\ \dot{x}_a \cos \theta + \dot{y}_a \sin \theta - L \, \dot{\theta} - r \, \dot{\varphi}_L = 0 \end{cases}. \tag{3.6}$$

The non-holonomic constraints equations can be combined into

$$\Lambda(\boldsymbol{q}) \, \dot{\boldsymbol{q}} = 0 \tag{3.7}$$

where

$$\Lambda(\mathbf{q}) = \begin{bmatrix} -\sin\theta & \cos\theta & 0 & 0 & 0 \\ \cos\theta & \sin\theta & L & -r & 0 \\ \cos\theta & \sin\theta & -L & 0 & -r \end{bmatrix}, \tag{3.8}$$

$$\dot{\boldsymbol{q}} = [\dot{x}_a \quad \dot{y}_a \quad \theta \quad \dot{\varphi}_R \quad \dot{\varphi}_L]^T \,. \tag{3.9}$$

In order for the AMR to turn, the velocity of the left and right wheels needs to be different. Therefore, a relationship between the AMR's linear and angular velocity of the left, $\dot{\varphi}_L$, and right, $\dot{\varphi}_R$, wheels can be established as

$$v = \frac{r\,(\dot{\varphi}_R + \dot{\varphi}_L)}{2}, \tag{3.10}$$

$$\omega = \frac{r\,(\dot{\varphi}_R - \dot{\varphi}_L)}{2L}. \tag{3.11}$$

So, the velocity of the centre point, A, can be defined in the robot frame of reference and the global frame of reference as

$$\dot{\boldsymbol{q}}^R = \frac{r}{2} \begin{bmatrix} 1 & 1 \\ 0 & 0 \\ \frac{1}{L} & -\frac{1}{L} \end{bmatrix} \begin{bmatrix} \dot{\varphi}_R \\ \dot{\varphi}_L \end{bmatrix}, \tag{3.12}$$

$$\dot{\boldsymbol{q}}^g = \frac{r}{2} \begin{bmatrix} -\cos\theta & \cos\theta \\ \sin\theta & \sin\theta \\ \frac{1}{L} & -\frac{1}{L} \end{bmatrix} \begin{bmatrix} \dot{\varphi}_R \\ \dot{\varphi}_L \end{bmatrix}. \tag{3.13}$$

The dynamic model is the study of the motion of the mechanical system considering forces that affect motion, and it is crucial for the simulation analysis of the mobile robot and for the design of some motion control algorithms (Dhaouadi and Hatab, 2013). Dynamics are defined using the Lagrange formula:

$$\frac{\mathrm{d}}{\mathrm{dt}}\left(\frac{\partial}{\partial \dot{q}_i}\right) + \frac{\partial L}{\partial q_i} = \mathbf{F} - \Lambda^T(\boldsymbol{q}) \, \boldsymbol{\lambda} \tag{3.14}$$

where $L = E_c - E_p$, E_c is the kinetic energy and E_p the potential energy of the robot; $\boldsymbol{q}_i$ are the generalized coordinates; $\boldsymbol{F}$ is the generalized force vector; Λ is the constraints matrix and $\boldsymbol{\lambda}$ is the Lagrange multiplier vector.

The total kinetic energy of the system is the sum of the kinetic energy of the left and right wheels (E_{cR} and E_{cL}, respectively) and the kinetic energy of the vehicle without wheels (E_{cC}). The kinetic energies are defined by:

$$
\begin{cases}
\mathrm{E_{cC}} = \dfrac{1}{2}\, m_C\, v_{wC} + \dfrac{1}{2}\, I_C\, \dot{\theta}^2 \\[2mm]
\mathrm{E_{cR}} = \dfrac{1}{2}\, m_w\, v_{wR} + \dfrac{1}{2}\, I_m\, \dot{\theta}^2 + \dfrac{1}{2}\, I_w\, \dot{\varphi}_R{}^2 \\[2mm]
\mathrm{E_{cL}} = \dfrac{1}{2}\, m_w\, v_{wL} + \dfrac{1}{2}\, I_m\, \dot{\theta}^2 + \dfrac{1}{2}\, I_w\, \dot{\varphi}_L{}^2
\end{cases}
\tag{3.15}
$$

where m_C is the mass of the mobile robot without the driving wheels, m_w is the mass of each driving wheel (with DC motors), I_C is the moment of inertia about the vertical axis through the centre of mass, I_m is the moment of inertia of each traction wheel (with DC motor) about the wheel diameter, I_w is the moment of inertia of each traction wheel (with DC motor) about the wheel axis (Dhaouadi and Hatab, 2013). Therefore, considering equations (3.2), (3.5) and (3.15), the total kinetic energy is

$$
\begin{aligned}
E_c = {} & \frac{1}{2}\, m\left(\dot{x}_a{}^2 + \dot{y}_a{}^2\right) - m_C\, d\, \dot{\theta}\left(\dot{y}_a \cos\theta - \dot{y}_a \sin\theta\right) + \frac{1}{2}\, I_w\left(\dot{\varphi}_R{}^2 + \dot{\varphi}_L{}^2\right) \\
& + \frac{1}{2}\, I\, \dot{\theta}
\end{aligned}
\tag{3.16},
$$

where $m = m_c + 2m_w$ and $I = I_C + m_C\, d^2 + 2m_w L^2 + 2I_m$. Considering equation (3.16) and the Lagrange formula, the equations of motion are the following

$$
\begin{cases}
m\, \ddot{x}_a - m\, d\, \ddot{\theta}\sin\theta - m\, d\, \dot{\theta}^2 \cos\theta = C_1 \\
m\, \ddot{y}_a - m\, d\, \ddot{\theta}\cos\theta - m\, d\, \dot{\theta}^2 \sin\theta = C_2 \\
I\, \ddot{\theta} - m\, d\, \ddot{x}_a \sin\theta + m\, d\, \ddot{y}_a \cos\theta = C_3 \\
\quad\quad I_w\, \ddot{\varphi}_R = \tau_R + C_4 \\
\quad\quad I_w\, \ddot{\varphi}_L = \tau_L + C_4
\end{cases}
\tag{3.17},
$$

where $(C_1,\ C_2,\ C_3,\ C_4,\ C_5)$ are coefficients related to the kinematic constraints and can be written in terms of the Lagrange multiplier vector (Dhaouadi and Hatab, 2013).

The dynamic model of a system with n generalized coordinates q subject to m bilateral constraints is defined by the following equation of motion:

$$
\mathbf{M}(\mathbf{q})\,\ddot{q} + V(q, \dot{q})\,\dot{q} = B(q)\,\tau - \Lambda^T(q)\,\lambda
\tag{3.18}
$$

where $\boldsymbol{M(q)}$ is the $n \times n$ inertia matrix, $\boldsymbol{V(q, \dot{q})}$ is the Coriolis and centrifugal matrix, $\boldsymbol{B(q)}$ is the input matrix (which is an identity matrix) and $\boldsymbol{\tau}$ is the input vector (torque of the driving wheels). These matrixes are described as

$$\mathbf{M(q)} = \begin{bmatrix} m & 0 & -m\,d\sin\theta & 0 & 0 \\ 0 & m & m\,d\cos\theta & 0 & 0 \\ -m\,d\sin\theta & m\,d\cos\theta & I & 0 & 0 \\ 0 & 0 & 0 & I_w & 0 \\ 0 & 0 & 0 & 0 & I_w \end{bmatrix} \qquad (3.19),$$

$$V(q,\dot{q}) = \begin{bmatrix} 0 & -m\,d\,\dot{\theta}\cos\theta & 0 & 0 & 0 \\ 0 & -m\,d\,\dot{\theta}\sin\theta & 0 & 0 & 0 \\ 0 & 0 & 0 & 0 & 0 \\ 0 & 0 & 0 & 0 & 0 \\ 0 & 0 & 0 & 0 & 0 \end{bmatrix} \qquad (3.20),$$

and

$$B(q) = \begin{bmatrix} 0 & 0 \\ 0 & 0 \\ 0 & 0 \\ 1 & 0 \\ 0 & 1 \end{bmatrix}. \qquad (3.21).$$

Since the Lagrange multiplier, λ, is unknown it is best to eliminate the constraint term $\Lambda^T(q)\,\lambda$ in equation (3.18) to aid the control and simulation process. First, the generalized coordinates are expressed according to the kinematic model:

$$\begin{bmatrix} \dot{x}_a \\ \dot{y}_a \\ \dot{\theta} \\ \dot{\varphi}_R \\ \dot{\varphi}_L \end{bmatrix} = \frac{1}{2} \begin{bmatrix} r\cos\theta & r\cos\theta \\ r\sin\theta & r\sin\theta \\ \dfrac{R}{L} & -\dfrac{R}{L} \\ 2 & 0 \\ 0 & 2 \end{bmatrix} \begin{bmatrix} \dot{\varphi}_R \\ \dot{\varphi}_L \end{bmatrix} \qquad (3.22).$$

This expression can also be defined as $\dot{q} = S(q)\,\eta$ where $\eta = [\dot{\varphi}_R \quad \dot{\varphi}_L]^T$. Moreover, the transformation matrix, $S(q)$, is the null space of the constraint matrix $\Lambda(q)$, so $S^T(q)\,\Lambda^T(q) = 0$. Therefore, when we derive the generalized coordinate vector defined in equation (3.13) and substitute these values in equation (3.18) we find the new dynamic equations (Dhaouadi and Hatab, 2013):

$$\bar{\mathbf{M}}(\mathbf{q})\,\dot{\eta} + \bar{V}(q,\dot{q})\,\eta = \bar{B}(q)\,\tau \qquad (3.23)$$

where

$$\bar{\mathbf{M}}(\mathbf{q}) = \begin{bmatrix} I_w + \dfrac{r^2}{4\,L^2}(mL^2 + I) & \dfrac{r^2}{4\,L^2}(mL^2 - I) \\ \dfrac{r^2}{4\,L^2}(mL^2 + I) & I_w + \dfrac{r^2}{4\,L^2}(mL^2 + I) \end{bmatrix} \qquad (3.24),$$

$$\overline{V}(q,\dot{q}) = \begin{bmatrix} 0 & \dfrac{r^2}{2\,L}\,m_C\,d\,\dot{\theta} \\ -\dfrac{r^2}{2\,L}\,m_C\,d\,\dot{\theta} & 0 \end{bmatrix}$$

(3.25),

$$\overline{B}(q) = \begin{bmatrix} 1 & 0 \\ 0 & 1 \end{bmatrix}$$

(3.26).

Thereby, we conclude that the dynamic model is only dependent on the angular velocities of each driving wheel, the angular velocity of the robot, and the driving motors' torque.

3.2. Locomotion Mechanism

After establishing all the basic requirements, the locomotion mechanism selection process begins. The motor, gearbox and wheels are the first components to be assessed and chosen, because they have a direct influence on subsequent decisions.

During early discussions, the challenge of developing a new differential system is proposed. In other words, the locomotion mechanism developed shall not be equipped with an omnidirectional drive configuration.

3.2.1. Driving Configuration

After some research and careful assessment, the characteristics of common driving configurations, presented in Section 2.2, are compared in Table 3.1.

Table 3.1. Advantages and disadvantages table for 3 non-holonomic drive configurations.

	Advantages	**Disadvantages**
Differential Drive	-Rotates on its axis. -Has four or six wheels.	-In irregular floors may lose traction.
Ackermann Steering	-Drives straight seamlessly.	-Cannot turn on its axis and requires a minimal radius. -The traction wheels may slip during turning.
Single-Wheel Drive	-Can rotate on its axis.	-Three-wheel configuration may not be stable enough.

The differential drive offers a better fit for this application because it allows for easy 360° movement, delivers good stability to move loads (with either four or six wheels), and also yields a proper suspension system to minimize the loss of traction. It is also among the most common drive configurations for industrial AMRs.

3.2.2. Wheels

As discussed in Section 2.2, differential drive requires two different sets of wheels: conventional/fixed and castor wheels. The number of wheels in AMRs of this type can vary. As stated before, with one castor wheel the robot is not able to turn on the spot. Hence, the choice between a four and six-wheeled AMR must be made.

The difference between these configurations lies in the stability when turning and load capacity. The six-wheeled option offers much more load capacity than the four-wheeled as weight is distributed through more wheels. Moreover, the six-wheeled configuration offers better stability especially when turning. Nevertheless, any mobile robot with more than three wheels must be equipped with a suspension system to ensure ground contact of all wheels in uneven terrains (Tzafestas, 2014b). For these reasons, the AMR is designed with six-wheels (two fixed wheels and four castor wheels).

The most relevant manufactures of wheels include Blickle® and TENTE®. Therefore, the wheels needed are chosen from their catalogues. The Blickle® public catalogue offers a "Wheel and castors guide" section that provides information on load capacity, manoeuvrability, floor preservation, wear resistance, rolling resistance and the characteristics of materials used on wheel threads. Hence, the sizing of the wheels is made

based on this catalogue. Before the wheel selection process can begin, the dynamic load capacity needs to be determined. The dynamic load capacity (T_D) is the mass a castor/wheel can withstand when tested on a rotating bench following DIN EN 12527-12533 (Blickle®, 2020). This can be calculated using the expression

$$T_D = \frac{E+Z}{n}\, S,$$

(3.27)

where E is the net mass of the transport equipment, Z is the load, n is the number of supporting wheels or castors, and S is the safety factor. The safety factor is given in the catalogue and is presented in ANNEX A.

Knowing the mass of the AMR and its maximum load along with the number of wheels needed, the dynamic load capacity, (T_D) can be determined using equation (3.27) as 48kg for fixed wheels and 5.3 kg for castor wheels, considering that the fixed wheels support 90% of the total AMR mass.

The diameter required for each type of wheel is defined based on typical parameterization for this application. Castor wheel diameters fall in range 50-100 mm, and fixed wheel diameters vary between 100-150 mm. Other parameters such as electrical conductivity (to avoid static energy build-up) and resistance to chemicals (especially chemicals present in hospital cleaning products) are important when choosing the wheels.

To further assess which chemicals the wheels should be resistant to, a list of chemical disinfectants used in hospitals is presented in APPENDIX A.

A spreadsheet containing all of the relevant information is created to facilitate the wheel selection process. Figure 3.3 shows the castor wheel section and Figure 3.4 shows the fixed wheel section of the spreadsheet.

#REF	Brand	D [mm]	L [mm]	H [mm]	Weight [kg]	Load Cap. [Kg]	Rolling resistance	Noise	Wear resistance	Corrosion resistance	RATING	Notes
7470YGO050P30-11	TENTE		20	69	0,152	50	3	3	3	5	3,5	Conductor
2470DIK050B10-11x3	TENTE		18	72	0,238	40	3	3	3	3	3,0	Conductor
2470UOK050P30-11	TENTE	50			0,189		4	3	5	3	3,8	Non-marking
7470PJH050P30-12,	TENTE		19	69	0,155	50	3	3	3	5	3,5	Non-marking
LRA-TPA 50G-ES	Blickle				0,2		4	3	3		3,3	Very high chemical resistance
LRA-TPA 50K-FK	Blickle				0,1		4	3	3		3,3	Very high chemical resistance
2470YGO075P30-11	TENTE				0,214	75	3	3	3	3	3,0	Conductor
2470YGO075P40	TENTE			100	0,245		3	3	3	3	3,0	Conductor
1470POO075P30-11	TENTE	75	25		0,213	40	3	3	5	3	3,5	Non-conductor
LRA-TPA 75K-ELS-Fl	Blickle			98	0,3		4	3	3		3,3	Conductor
LPA-TPA 75K-ELS-Fl	Blickle			100	0,3	50	4	3	3		3,3	Conductor; Non marking
LHF-ALEV 100K-1-S(	Blickle			175			4	4	4		4,0	Initial tension: 30Kg; Non-marking
LHF-ALST 100K-1	Blickle	100	40		3,7	200	4	4	4		4,0	Initial tension: 30Kg; Non-marking
LPFE-ALEV 100K-FA	Blickle			170			4	4	4		4,0	Initial tension: 40Kg

Figure 3.3. Castor wheel selection spreadsheet.

Fixed Wheels												
#REF	Brand	D [mm]	L [mm]	d [mm]	Weight [kg]	Load Cap. [Kg]	Rolling resistance	Noise	Wear resistance	Corrosion resistance	RATING	Notes
TPA 126/8K-ELS-FK	Blickle		36	8	0,3	80	4	3	3		3,3	Conductor; Ball bearing
TPA 127/12G-ELS	Blickle		45	12	0,2		4	3	3		3,3	Conductor; Sleeve bearing
PJP125x32-Ø8 Rk. 9l	TENTE	125		8	0,276		3	3	3	3	3,0	Non-conductor; Ball bearing
PJC125x32-Ø8	TENTE		27		0,281	100	3	3	3	3	3,0	Non-conductor; Ball bearing
YGO125x32-Ø12	TENTE		35	12	0,237		3	3	3	3	3,0	Conductor; Sleeve bearing
VPA 125/8K-EL	Blickle			8	0,3	75	3	4	4		3,7	Conductor; Ball bearing
GSTN 127/25H7	Blickle		60	25 H7	1,85	400	4	4	4		4,0	Tread material: Softhane; Non-conductor
GTHN 125/20H7	Blickle	125	40	20 H7	1,537	450	4	3	3		3,3	Tread material: Extrathane; Non-conductor
GBN 127/25H7	Blickle		60	25 H7	1,82	650	5	3	3		3,7	Tread material: Besthane; Non-conductor

Figure 3.4. Fixed wheel selection spreadsheet.

The rating system shown in Figure 3.3 and Figure 3.4 is taken from the companies' rating system and so cannot be used to accurately compare wheels between companies. The final rating is the mean value of the parameters shown.

According to Blickle® (2020), rolling resistance is defined as the amount of force required to keep the wheel moving uniformly. The noise parameter relates to floor preservation and smooth operation; the higher the score in this category, the quieter the wheel is and the easier it is on surfaces.

Initially, we chose 50 mm castor wheels and 100 mm fixed wheels, but upon discussion decided to increase the diameter of the wheels. Bigger wheels can withstand more weight and have better rolling resistance. So, the diameter of the wheels is adjusted to 75 mm for castors and 125 mm for fixed wheels.

Blickle® wheels are ultimately chosen for this project because of the abundance of information available in their website and catalogue. With this information, we are able to make a better comparison between wheels and take a more substantiated decision.

The castor wheel chosen is LPA-TPA 75K-ELS-FK, marked in green in Figure 3.3. It is electrically conductive and has sufficient dynamic load capacity. The wheel tread is made from thermoplastic rubber-elastomer (TPE), which according to the catalogue allows for smooth operation, good rolling resistance and satisfactory wear resistance. The TPE is also resistant to formaldehyde and sodium hypochlorite.

Castors equipped with a suspension (steel spring) are also considered, marked grey in Figure 3.3. However, the initial tension on the spring was bigger than the weight supported by the castors. This meant that the initial tension would never be overcome and so the spring would not be able to function properly. For this reason, this option is discarded, and a new suspension system is designed.

As for fixed wheels, the VPA 125/8K-EL is firstly chosen. It too complies with the dynamic load and electrical conductivity requirements. However, after designing the AMR, we noticed that the fixed wheel initially chosen was not equipped with a keyway but

rather a ball bearing. As a result, we would not be able to fix the wheel to the gearbox shaft and so the AMR would not manage to move. Thus, a new selection process is done for traction wheels, which are equipped with keyways. From the three final choices available, GSTN 127/25H7 was chosen. Since all three wheels had similar characteristics, the key factors are: rating, dynamic load capacity and chemical resistance of the tread material. GSTN 127/25H7 has the lowest load capacity and the best rating. As for chemical resistance, it performs slightly worse than the GBN 127/25H7, wheel but not so much so as to be considered relevant. On a last note, GSTN 127/25H7 has a cast iron core and so a special request for a stainless-steel wheel core needs to be filed.

3.2.3. Motor and gearbox

The type of electric motor most suited for this application is the Brushless DC motor. This motor has the highest power density and efficiency and no wearing components, which is optimal for this application where weight/efficiency ratio is critical. The absence of wearing components also allows for the need for less maintenance, which is key for the AMR.

Motor assessment requires calculating the needed torque. Torque (T) is calculated by

$$T \, (\mathrm{N\,m}) = \frac{9555 \, P \, (\mathrm{W})}{n_m \, (\mathrm{rpm})}$$

(3.28),

where P is the power of the electric motor and n_m is the velocity of the motor. The velocity of the motor is known, but power needs to be calculated. It is also known that power is the moment of the motor (M_m) times the angular velocity of the motor (ω_m):

$$P = M_m \, \omega_m$$

(3.29).

In turn, the moment is determined through the Law of Conservation of Kinetic Energy defined in the differential form as

$$\frac{dE_c}{dt} = \frac{dW_{ext}}{dt} + \frac{dW_{int}}{dt}$$

(3.30),

where W_{ext} is the external work, W_{int} is the internal work, E_c is the kinetic energy and t is time. For the AMR motors, the power of the gearbox results in internal work and the friction

force (F_a) caused by the wheels results in external work. So, when developing equation (3.30) we get

$$\frac{d(\frac{1}{2} m \, v^2)}{dt} = \mu_{gb} \, P - F_a \, v \tag{3.31},$$

where v is the velocity of the gearbox and consequently the velocity of the AMR and μ_{gb} is the efficiency of the gearbox.

The parameters known are the following:

- Efficiency of the gearbox, μ_{gb}: 0.8;
- Initial acceleration, a: 0.5 m s^{-1};
- Wheel radius, r: 62.5 mm;
- Rolling resistance coefficient, μ_c: 0.04;
- Gearbox ratio, i: 16;
- Gravitational acceleration, g: 9.81 m s^{-2};
- Mass of the AMR, m: 200 kg;
- Angular velocity of the motor, n_m: 2500 rpm.

After choosing the motor and respective gearbox, μ_{gb} and i have to be adjusted. Thus, the torque needs to be calculated again to assure the motor chosen functions correctly. Moreover, these known parameters are estimated, but correspond to mean values for AMRs, according to the expertise of AST.

The AMR has translation movement but also rotation movement from the wheels and components in rotation in the motor and gearbox. Therefore, the kinetic energy is defined by

$$E_c = \frac{1}{2} m \, v^2 + \frac{1}{2} I_z \, \omega^2 \tag{3.32},$$

where m is the mass of the AMR, v is the linear velocity, I_z is the moment of inertia of rotating masses, and ω is the angular velocity. Since there is a great deal of rotating components in the AMR, it is impractical to calculate I_z. Instead, another approach is done. Equation (3.32) is simplified into

$$E_c = \frac{1}{2} m_{eq} \, v^2 \tag{3.33},$$

where m_{eq} is the equivalent mass when the AMR is in motion. According to the expertise of Professor Fernando Antunes, the total inertia of rotating masses for motorised applications

is 3 % - 5 % of the translational inertia. Considering that the total inertia is 5 % of the translational inertia the equivalent mass is 210 kg.

The next step is solving equation (3.31). The friction force can be determined as

$$F_a = \mu_c\, m\, g \tag{3.34}.$$

So,

$$m\, v\, a = \mu_{gb}\, P - \mu_c\, m\, g\, v \tag{3.35}.$$

The velocity of the gearbox can be estimated with the gearbox ratio because the ratio is the motor angular velocity (ω_m) divided by the wheel angular velocity (ω_r),

$$\omega_r = \frac{\omega_m}{i} \tag{3.36}.$$

Thus, $\omega_r = 16.36$ rad s^{-1}.

Moreover, the linear velocity, v can be found by the following expression:

$$v = \frac{\omega_m}{i}\, r \tag{3.37}$$

Hence, $v =1.023$ m s^{-1}. From equation (3.35) we can extrapolate the value of P as 239.64 W. The power determined is the power of the two electric motors combined. So, the power required for one motor is $P_{sm} = 119.82$ W. Finally, using equation (3.28) the single motor torque is determined as $T = 0.458$ N m.

After calculating the needed toque, three motor brands (Dunkermoteren®, Nanotec® and Beckhoff®) are inquired in order to find the optimal motor for the application. The selection process is done through another spreadsheet (Figure 3.5). To select possible motors a few key characteristics, need to be considered:

- Voltage: 24 V;
- Communication Protocols;
- Safety Protocol of at least STO (Safety Torque Off) when the motor has a controller incorporated;
- Weight;
- Size;
- Torque (bigger than the torque previously calculated).

Motor									
#REF	Brand	T [N.m]	P [W]	n [rpm]	Length [mm]	Weight [kg]	Communication Protocol	Controller / Encoder	STO
BG 65x75 dMove	Dunkermoteren ▾	49	187	3650	165	2	CANopen / RS485	YES / NO	NO
BG 66x50 dMove B	Dunkermoteren ▾		206	3520					
BG 66x50 dPro	Dunkermoteren ▾	0.56	206 -446	3520-3350	140	1.65	CANopen / IO stand alone OR Profinet / EtherCAT (opt.) / Ethernet/IP (opt.)		YES
DB43L024030-A	Nanotec ▾	0.3	94	3000	80.3	0.8	-	NO / NO	-
DB59M024035R-A	Nanotec ▾	0.37	135	3500	68.6	0.65	-		-
AMI8122	Beckhoof ▾	0.78	163	2000	177	-	EtherCAT	YES / OPT.	YES
DB59L024035R-B3	Nanotec ▾	0.47	172	3500	73.6	0.72	-	NO / NO	-

Figure 3.5. Selection process of the motor.

Dunkermoteren® motors are eliminated first because they are large, heavy, and some do not have the STO function. The Beckhoff® motor is a servo drive, which means it has a controller integrated. This motor is eliminated too because it is large, and its torque and power are bigger than needed. Nanotec® motors are compact, lightweight and can include gearboxes, encoders, and brakes. This is beneficial because it can save time and money when shipping and mounting since all components are assembled by Nanotec®. For these reasons, Nanotec® motors are chosen. So, the motor initially chosen and with the best trade-off is the Nanotec® BD59M024035R-A.

Upon choosing the motor, the gearbox brake and encoder need to be selected. The Nanotec® website has a product configurator that allows us to combine the appropriate components to the motor. The brake is the first to be chosen since there is only one brake available for BD59M024035R-A. The BRAKE-BWA-1,5-6,35 is the designated holding brake of the motor. It is a power-off brake which means that it is activated when the electric current is removed. These types of brakes are used in parking or emergency stop because, for example, they are activated when the AMR is powered down.

When it comes to encoders, there are three magnetic encoders available. They vary in signal type, resolution, operating voltage, and height. Incremental encoders can only count from zero. Therefore, it requires referencing after it is turned on or after a failed recovery. Incremental encoders can locate a certain absolute position of the motor shaft but may not return the exact position of a wheel. Synchronous Serial Interface (SSI) encoders are digital encoders where the converted data is read bit by bit from the sensor (Bräunl, 2003). This means these encoders provide an absolute position with great resolution at very fast update rates (Roboteq®, 2018). For these, the SSI encoder, NME2-SSI-V06-12-C is chosen.

Finally, the gearbox is selected. Since the gearbox ratio falls between 15 and 20, we gathered the Nanotec® gearboxes within this transmission ratio interval, as seen in Figure 3.6.

Gearbox							
#REF	Reduction Ratio	Efficiency [%]	Rated Torque [Nm]	Length [mm]	Weight [kg]	Life [h]	Notes
GP56-S2-16-SR	15.51	89	24.6	61.8	0.84	10000	Protection: IP54; Standard Bearing
GP56-T2-16-HR		94		66	0.93		Protection: IP54; Reinforced Bearing
GP56-N2-16-SR	15.61	86	7.4	67	0.83	5000	Protection: IP54; Standard Bearing
GP56-S2-20-SR	20.03	89	28.6	61.8	0.79	10000	
GP56-T2-20-HR		94		66	0.88		Protection: IP54; Reinforced Bearing

Figure 3.6. Nanotec gearboxes applicable for the motor chosen.

The last two gearboxes shown in Figure 3.6 are the first to be eliminated since their reduction ratio is higher than 20. Gearbox GP56-N2-16-SR has a significantly shorter operating life than the other gearboxes selected so this one is to be discarded. The first two gearboxes are very similar. The only differences are efficiency, length, and weight. Considering that the AMR has to be as light and compact as possible, GP56-S2-16-SR (marked green in Figure 3.6) is an optimal choice.

So, with all of the components selected, the sizing calculations for the motor have to be adjusted:

- Efficiency of the gearbox, μ_{gb}: 89 %;
- Gearbox ratio, i: 15.51.

Using Equations (3.28), (3.36) and (3.37), the angular and linear velocities of the wheel are now $\omega_r = 16.879$ rad s^{-1} and $v = 1.055$ m s^{-1}, respectively. Furthermore, the power of the motors is $P = 222.147$ W. Thus, the motors have a power of 111.07 W and a torque of 0.42 N m each.

With these new torque and power requirements, we need to verify if the motor chosen is still viable. For that, we consulted the torque/speed characteristics graph available in Nanotec® (2018). The motor initially chosen, BD59M024035R-A, has a rated speed of 3500 rpm and a rated torque of 0.37 N m. The speed of the AMR is much lower than the rated speed while the torque needed is higher than the rated torque. This means that the motor initially chosen would function in the "Intermittent Torque Zone" (Figure 3.7). When a motor operates in this zone, it cannot operate continuously without causing damage. Hence, another motor with a higher rated torque needs to be selected for the motor to operate in the "Continuous Torque Zone".
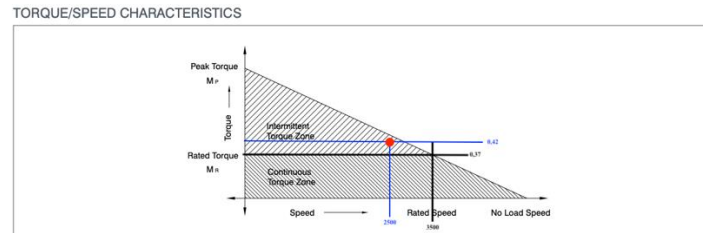
Figure 3.7. BD59M024035R-A torque/speed graph. Black lines: rated values; blue lines: required values; Nanotec (n.d.).

The next DB59 motor with the closest rated torque value is the DB59L024035R-B3 (marked dark green in Figure 3.5). This motor has the same properties as the one initially chosen but has a rated torque of 0.47 N m. Since DB59L024035R-B3 belongs to the same series as the motor initially chosen, the other components are compatible and do not have to be re-selected.

In conclusion, the components chosen are:

- Motor: DB59L024035R-B3 from Nanotec[®];
- Gearbox: GP56-S2-16-SR from Nanotec[®];
- Brake: BRAKE-BWA-1,5-6,35 from Nanotec[®];
- Encoder: NME2-SSI-V06-12-C from Nanotec[®].

3.2.4. Suspension

The ideal suspension system aims only to assure that traction wheels are always in contact with the ground. Initially, it was considered a design based on the work of Borvorntanajanya et al. (2016). They devised a system with four-bar linkages and gas springs (Figure 3.8). This system is also coupled with a universal joint so the wheel can move up and down.
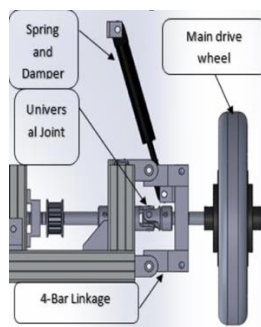
Figure 3.8. The suspension system designed by Borvorntanajanya et al. (2016)**.**

We also researched the suspension systems used in automobiles. The most common concepts seen in cars are the MacPherson strut and double-wishbone suspension (DWB). DWB is typically used in high-performance cars and SUVs (Reddy et al., 2016). The MacPherson strut suspension is more compact and compatible with transversely mounted motors than the DWB and is commonly used in front-wheel-drive cars (Reddy et al., 2016).

The first concept for the AMR combines the MacPherson strut suspension with the design developed by Borvorntanajanya et al. (2016). The design is depicted in Figure 3.9 and shows the traction wheel and its shaft connected to a universal joint. This joint links the wheel to the gearbox shaft to enable the wheel to move up and down as it passes through obstacles. On the wheel shaft, there is a separate knuckle to attach the shock absorber and the link to the chassis. This knuckle is equipped with roller bearings so the shaft can easily turn. Upon discussion of this option, a few problems appeared. This system was very lengthy and made it impossible to position the two motors back-to-back. The universal joint was simple and did not compensate for the difference in length when the wheel travels up and down. Shock absorbers, despite widely used, have gas dampers that are prone to lose strength over time and require significant maintenance. They are also used to make the ride as smooth and comfortable as possible. Since the AMR is unmanned, travelling at low speeds and indoors, gas dampers are not necessary.
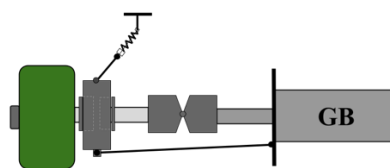
Figure 3.9. Conceptual drawing of the second suspension design. The gearbox is connected to the wheel shaft through the universal joint.

The second and final concept is an upgraded version of the first design. The universal joint was replaced by a telescopic universal joint. The separate knuckle is redesigned to accommodate the compression spring in the vertical position. The wishbone is also removed because the knuckle is already secured axially by the wheel shaft. Figure 3.10 shows the schematics for this option.
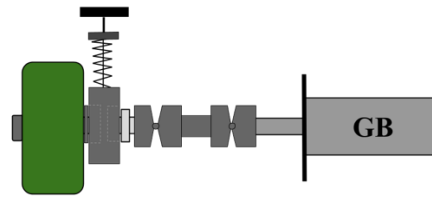
Figure 3.10. Conceptual drawing of the third suspension design. The gearbox is connected to the wheel shaft through the telescopic joint. The suspension knuckle is secured axially by a washer and the wheel shaft.

For the spring housing, there are also two iterations illustrated in Figure 3.11. The first design (A) is conceived with a spacer tube paired with a guide pin for support. Inside the spacer tube lies a bushing to enable the pin to move up and down. Since the spring is positioned above the spacer tube this solution proved to be very lengthy and thus ineffective. The concept in Figure 3.11B is created to mitigate the length problem of the previous design. A tapered bolt fixed to the lower plate is used as a guide pin. The spring is mounted around the bolt and between the plates. In this configuration, bushings are necessary to ease the movement of the bolt. This solution is simple and compact.

(A)　　　　(B)
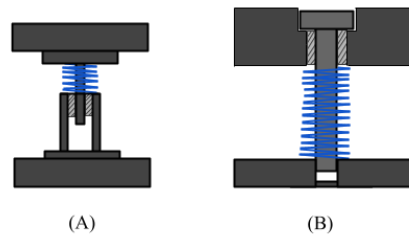
Figure 3.11. Three iterations of the spring housing: A – spacer tube housing; B – bolt housing.

The wheel shaft is sized using the Design Accelerator® tool in Autodesk Inventor®. The wheel shaft has a keyway and a bolted connection to secure the shaft to the wheel. Both these components are sized separately by the Design Accelerator® tool.

Figure 3.12 shows how the wheel shaft is sized. The shaft is made from stainless steel and the forces being applied to it are: engine torque, spring force, wheel friction force and wheel radial force, from left to right in Figure 3.12.
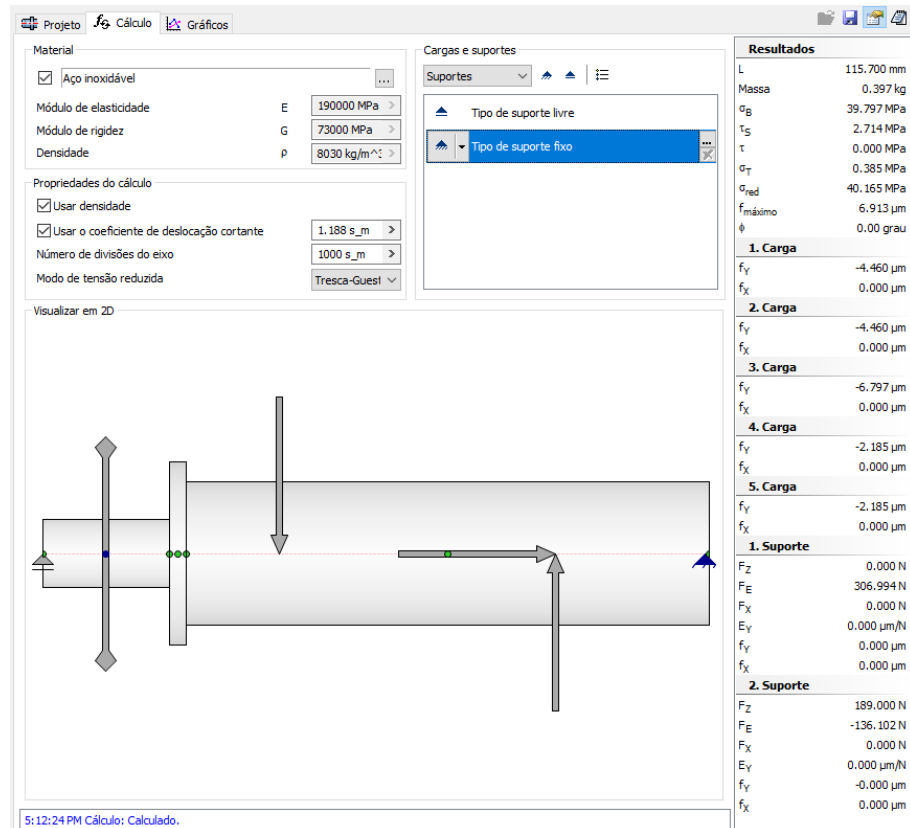
Figure 3.12. Design Accelerator® tool calculations for the wheel shaft. The blue words at the bottom mean that the calculations are successful.

The keyway Design Accelerator® calculations are shown in Figure 3.13. This keyway (DIN 9885-1 A 8×7-45) is located on the wheel at one end of the shaft. In Figure 3.13 the materials of the shaft, keyway, and wheel bore are defined. The loads are also defined from the motor and gearbox sizing. The load factors on the lower bottom corner of Figure 3.13 are established for a uniform load with light impacts.
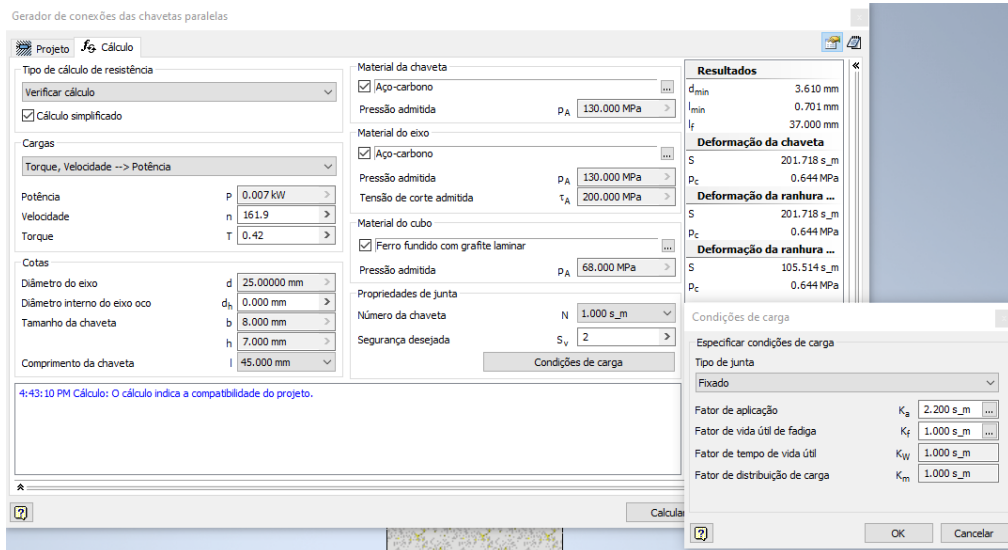
Figure 3.13. Design Accelerator® tool calculations for the wheel keyway. The blue words at the bottom mean that the calculations are successful.

The bolted connection of the shaft and wheel is also sized using the Design Accelerator® tool. The bolted connection is composed of an ISO 4017 M12×30 hexagonal bolt and a DIN EN ISO 7093-2 12 washer. In Figure 3.14 the materials, loads, and calculation factors are defined. Thus, the bolt is statically sized with a safety factor of 13.
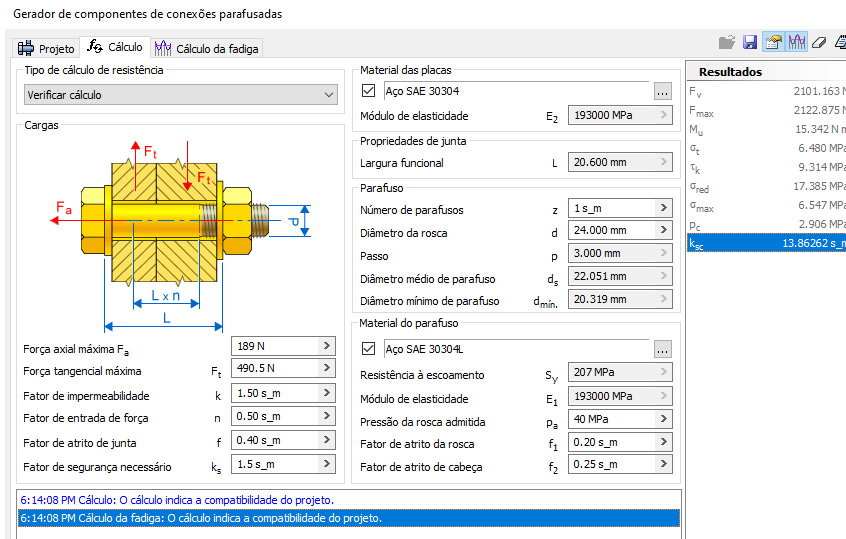
Figure 3.14. Design Accelerator® tool calculations for the bolted connection. The blue words at the bottom mean that the calculations are successful.

Bolts also need to be sized in terms of fatigue. Thus, in Figure 3.15 we use the Soderberg method with a fluctuated load to reach a safety factor of 174.
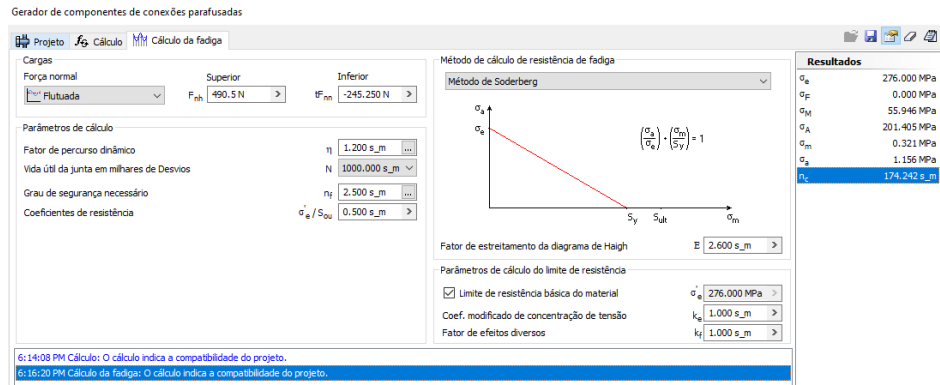
Figure 3.15. Design Accelerator® tool fatigue calculations for the bolted connection. The blue words at the bottom mean that the calculations are successful.

The telescopic universal joint chosen, 23412-120260, is from norelem®. It is compatible with the gearbox shaft and its length can be customized. The standard length of this component is 260 mm but when we adjust the length of the sliding sleeve, its length comes down to around 150 mm.

The spring chosen is sized from the Fibro® catalogue. Regarding compression springs, Fibro® produces four (blue, green, yellow, and red) that follow the DIN ISO 10243 standard. In order to size the spring with the longest life possible, the spring compression ratings had to be within a specific interval illustrated in Figure 3.16.
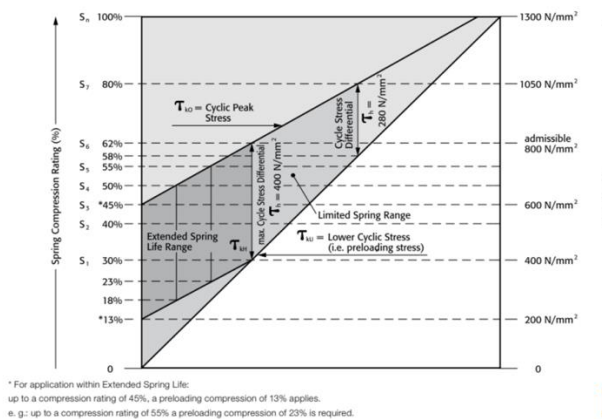
Figure 3.16. Time and spring life diagram. The longest life is achieved in the "Extended Spring Life Range" area in dark grey (Fibro® 2021)

The spring compression ratings ("S_1… S_n" in Figure 3.16) measure, in percentage, by how much the spring has been compressed. S_1 relates to when the spring is mounted, but not yet under any external force. S_2 to S_7 are the spring paths assigned to spring forces and S_n is the spring path when it is 100 % compressed. The preloading force and

respective spring path are smaller than S_1, because when the spring is mounted it tends to suffer a small compression.

The preloading force of the spring (F_m) needs to be higher than the radial force acting on the wheel. The radial force (N) is a result of the friction force acting on the wheel and it is defined by

$$N = \frac{F_a}{\mu_e} \tag{3.38}$$

where F_a is the friction force and μ_e is the static coefficient of friction. To determine the friction force, a force diagram (Figure 3.17) is done. The diagram shows all the forces and moments acting on the wheel.
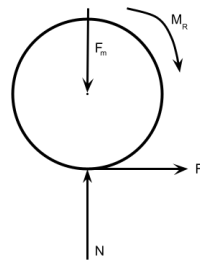
Figure 3.17. Force diagram of the forces acting on the wheel. F_m is the spring preloading force and M_R is the moment of the wheel

The moment on the wheel (M_R) can be calculated as the multiplication of the moment of the motor (M_m) and the gearbox ratio (i):

$$M_R = M_m \, i \tag{3.39}$$

but also, can be defined as

$$M_R = F_a \, r. \tag{3.40}$$

The power of the motor is already known from the characteristics of the motor chosen in Figure 3.5. Although the motor has a power of 172 W, the spring was sized for a motor of 200 W for safety purposes. Therefore, using equation (3.29) we can determine the moment of the motor as M_m =0.76 N m. The moment of the wheel can be found from equation (3.39) as M_R =11.85 N m.

Since the wheel has a radius of 62.5 mm the friction force derived from equation (3.40) is F_a =189.6 N.

The static coefficient of friction is dependent on the tread material and the material with which it is in contact with. The most common materials for hospital floor finishing are vinyl composite tile, rubber, linoleum, and ceramic flooring (Singh, 2017). The

wheel tread is made from a polyurethane elastomer Blickle Softhane® with a hardness of 75 Shore A. The exact static coefficient of friction for these materials is not known but we can reach an approximate value. The static coefficient of friction between a thermoplastic polyurethane (40-85 Shore A) and ceramic tiling is between 0.4 and 1 (Caetano, 2019). Therefore, the static coefficient of friction between the tread material and hospital flooring is defined as $\mu_e = 0.45$. Using Equation (3.38), the radial force is N = 421.3 N.

With the minimal preloading force determined, the spring sizing is conducted through an iteration process. Using Hooke's Law and the spring compression rates, an excel sheet is constructed. In this spreadsheet, spring course, length, preload force and end course force are analysed to determine the optimal spring. Parameters such as stiffness constant, maximum stoke and rest length when there is no force being applied are retrieved from the Fibro® catalogue. This selection process is represented in Figure 3.18 and is conducted with the following steps:

1. Calculation of the spring course. The spring course is the subtraction of the pre-compression (spring path when the pre-loading force is applied) and end course compression (spring path when the end course force is applied);

2. Calculation of the spring length when the pre-loading and end course forces are applied;

3. Calculation of the pre-loading and end course forces using Hooke's Law.

Colour	Reference	Course [mm]	Length (free) [mm]	Preload length [mm]	Negative end course length [mm]	End course length [mm]	Length when 100% compressed [mm]	Minimal compression [%]	Maximum compression [%]	Preload Force [N]	End course Force [N]	FITS?
	#REF	x	L0	L1	Lm	Ln	Lmax					
GREEN	241.14.25.152	11,4	152	129,2	140,6	117,8	76	30,00%	45,00%	319,2	478,8	NO
BLUE	241.15.25.152	22,8	152	130,6	153,4	107,8	80,7	30,00%	62,00%	444,9	919,5	YES
RED	241.16.25.152	13,1	152	142,3	155,4	129,2	95	17,00%	40,00%	463,2	1089,8	NO
YELLOW	241.17.25.152	7,1	152	144,9	152,0	137,8	104,5	15,00%	30,00%	452,4	904,9	NO
GREEN	241.14.25.139	20,9	139	118,2	139,0	97,3	69,5	30,00%	60,00%	319,0	638,0	NO
BLUE	241.15.25.139	9,8	139	119,5	129,2	109,7	73,9	30,00%	45,00%	453,1	679,6	NO
RED	241.16.25.139	6,8	139	130,1	136,9	123,4	86,9	17,00%	30,00%	466,8	823,7	NO
YELLOW	241.17.25.139	7,4	139	132,5	139,9	125,1	95,6	15,00%	32,00%	429,7	916,6	NO
YELLOW	241.17.63.178	5,5	178	161,5	167,0	156,0	123	30,00%	40,00%	409,2	545,6	NO
YELLOW	241.17.25.178	8,3	178	169,7	178,0	161,3	122,4	15,00%	30,00%	449,5	899,1	NO
RED	241.16.25.178	10,0	178	166,0	176,0	156,0	111,2	18,00%	33,00%	493,0	903,8	MAYBE
BLUE	241.15.25.178	26,7	178	153,0	179,7	126,3	94,6	30,00%	62,00%	445,4	920,4	YES
GREEN	241.14.25.178	13,4	178	151,3	164,7	138,0	89	30,00%	45,00%	333,8	500,6	NO
GREEN	241.14.25.127	9,5	127	108,0	117,5	98,4	63,5	30,00%	45,00%	318,1	477,2	NO
BLUE	241.15.25.127	10,1	127	109,2	119,3	99,0	67,5	30,00%	47,00%	462,3	724,3	YES

Figure 3.18. Spreadsheet for sizing the spring. The spring chosen is highlighted in orange.

To have a spring with an extended life cycle the compression rates are kept within the interval set in Figure 3.16. Moreover, the end-course force is also limited to a maximum of 1 kN, which is the amount of force required to lift the AMR off the ground.

There are four springs, highlighted in green and yellow in Figure 3.18, that fulfil the spring course, pre-load force and end-course force requirements. Spring 241.15.25.127 is chosen since it is the most compact and can withstand the majority (73 %) of the total weight.

Tapered roller bearings are fit for applications with combined loads (radial and axial forces acting simultaneously). When it comes to a rotating component, such as short shaft, two bearings are used to support and position the component radially and axially relative to the stationary part. Back-to-back and face-to-face arrangements can support axial loads in both directions, but the back-to-back arrangement can accommodate tilting moments while the face-to-face can accommodate slight misalignments (SKF®, 2018). The wheel shaft travels up and down and induces tilting moments on the shaft and consequently on the bearings. For this reason, tapered roller bearing arranged back-to-back are used.

Bearings are sized statically and dynamically. Dynamic sizing is characterized by rating life while static sizing is determined by the static safety factor (S_0):

$$S_0 = \frac{C_0}{P_0},$$ (3.41)

where C_0 is the static basic load rating and P_0 is the equivalent static load. Considering that we are using SKF® bearings with SKF® rating life, which complies with ISO 281. The SKF® rating life is defined by:

$$L_{nmh} = \frac{10^6}{60\,\omega}\, a_1\, a_{SKF}\, \left(\frac{C}{P}\right)^p,$$ (3.42)

where L_{nmh} – SKF® rating life at (100-n) % reliability (in hours); n – failure probability; a_1 - life adjustment factor for reliability, a_{SKF} – SKF® life modification factor; C – basic dynamic rating load; P – equivalent dynamic bearing load; ω – rotational speed; p – exponent of the life equation (p =3 for ball bearings and p =10/3 for roller bearings).

We can establish the reliability of the bearings at 98 %. So, according to (SKF® 2018), the failure probability, n, and life adjustment factor for reliability, a_1, are 2 and 0.37, respectively.

The equivalent dynamic bearing load, P, for the back-to-back arrangement is determined by:

$$\begin{aligned}
{F_a}/{F_r} \le e &\rightarrow P = F_r \\
{F_a}/{F_r} > e &\rightarrow P = 0.4\, F_r + Y \cdot F_a
\end{aligned}$$ (3.43),

where F_a – axial load; F_r – radial load; e, Y – calculation parameters. The equivalent static load is defined as:

$$\begin{cases} P_0 = 0.5 \cdot F_r + Y_0 \, F_a \\ P_0 < F_r \rightarrow P_0 = F_r \end{cases}$$

(3.44).

When radial loads are applied to tapered roller bearings, the load is transmitted from one raceway to another at an angle to the bearing axle and it induces an axial force (SKF®, 2018). The forces acting on the bearings are the spring force, F_m, wheel radial force, N, and wheel friction force, F_a. Since these forces do not act on the same plane, the radial and axial forces of the bearings have to be determined by combining the YZ (Figure 3.19) and XZ (Figure 3.20) plane.

In the case of the tapered roller bearings, as stated before, the radial load is transmitted at an angle and therefore we cannot represent the reaction radial force on the centre of the bearing but rather at the pressure point.

On the YZ plane, the reaction radial force is calculated through the analyses of the free body diagram in Figure 3.19.
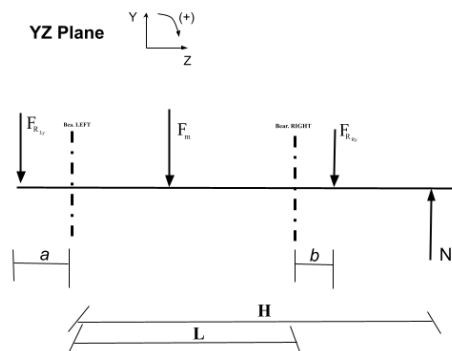
Figure 3.19. Free body diagram of the YZ plane.

The distance between the bearings, L, and the distance from the bearing to the wheel, H, are retrieved from the CAD drawings of the AMR. When designing the AMR in AutoCAD Inventor® and attending to the space constraints of the model we concluded that L and H are both 42 mm. The distances between the centre of the bearing and the pressure point (a, b) are given on the product tables.

Hence, the reaction bearing forces ($F_{R_{Ly}}$ and $F_{R_{Ry}}$) are defined by:

$$\begin{cases} F_{R_{Ly}} = F_m + F_{R_{Ry}} - N \\ F_{R_{Ry}} = \dfrac{N(H+a) - F_m\left(L/2 + a\right)}{L+b+a} \end{cases} \tag{3.45}.$$

Since the spring force is not constant, SKF® (2018) states that the mean load within a duty interval is

$$F_{med} = \frac{F_{min} + 2\,F_{max}}{3} \tag{3.46}.$$

The spring forces calculated define the minimum and maximum loads in the duty interval of equation (3.46). Therefore, $F_{med} = 641$ N.

On the XZ plane (Figure 3.20), only the wheel friction force is acting on the bearings.
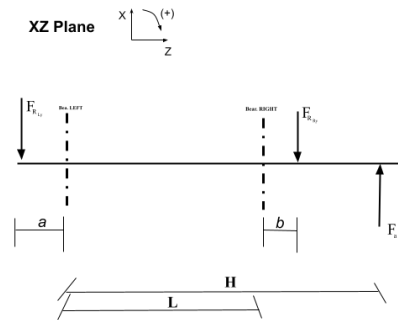
Figure 3.20. Free body diagram of the XZ plane.

Therefore, the radial bearing loads ($F_{R_{Lx}}$ and $F_{R_{Rx}}$) are:

$$\begin{cases} F_{R_{Lx}} = F_{R_{Rx}} - F_a \\ F_{R_{Rx}} = \dfrac{F_a(H+a)}{L+b+a} \end{cases} \tag{3.47}.$$

The roller bearings need to have an internal diameter of at least 25 mm as the wheel has an axle bore of 25 mm. Thus, we selected the first two roller bearings from the SKF® catalogue with an internal diameter of 25 mm: 32005X (on the left) and 30205 (on the right). With the data retrieved from the SKF® catalogue, we can calculate the values of the radial bearing loads from equation (3.45) and equation (3.47):

$$\begin{cases} F_{R_{Lx}} = -469\text{ N} \\ F_{R_{Rx}} = 302\text{ N} \\ F_{R_{Ly}} = -58\text{ N} \\ F_{R_{Ry}} = 247\text{ N} \end{cases} \cdot \tag{3.48}.$$

Therefore, the total radial load acting on the left roller bearing is:

$$\begin{cases} F_{R_L} = 472 \text{ N} \\ F_{R_R} = 39 \text{ N} \end{cases}$$

(3.49).

The axial bearing loads are calculated depending on the bearing application and load case. SKF® (2018) provides a table, shown in Figure 3.21, with the necessary equations for each load case.

Figure 3.21. Axial bearing loads equations for different applications with two single row tapered roller bearing arrangements (SKF®, 2018).

There is no external axial force (K_A) acting on the wheel shaft of the AMR. The load case is calculated with the radial forces defined in Equation (3.49) and the roller bearing calculation factors given in SKF® (2018)

$$\begin{cases} \dfrac{F_{R_L}}{Y_L} = 0.337 \\ \dfrac{F_{R_R}}{Y_R} = 0.244 \end{cases}$$

(3.50).

Therefore,

$$\frac{F_{R_L}}{Y_L} > \frac{F_{R_R}}{Y_R}$$

(3.51).

For these reasons the load case is "Case 2c". The axial loads are the following:

$$\begin{cases} F_{a_L} = 169 \text{ N} \\ F_{a_R} = 169 \text{ N} \end{cases} \tag{3.52}.$$

The equivalent dynamic bearing loads can now be calculated using the values of the radial forces in equation (3.49) and the values of the axial forces in equation (3.52). Considering equation (3.44) that

$$\begin{cases} {}^{F_{a_L}}\!/\!_{F_{r_L}} = 0.358 \; < 0.43 \\ {}^{F_{a_R}}\!/\!_{F_{r_R}} = 0.433 \; > 0.37 \end{cases} \tag{3.53},$$

then, $P_L = 47$ N and $P_R = 43$ N.

As for the equivalent static bearing load, the values are:

$$\begin{cases} P_{0_L} = 371 \text{ N} \\ P_{0_R} = 347 \text{ N} \end{cases} \tag{3.54}.$$

However, the values calculated in equation (3.54) are lower than the respective radial forces. So, according to equation (3.44), $P_{0_L} = 472$ N and $P_{0_R} = 390$ N.

The static safety factor can now be found using equation (3.41) for the left bearing and the right bearing: $S_{0_L} = 68.8$ and $S_{0_R} = 68.8$, respectively. With these high safety factors, the bearings are statically fit.

Before calculating the rating life, the life modification factor (a_{SKF}) needs to be determined. This factor is dependent on the level of contamination of the bearing (η_c), the lubrification condition (κ) and the relation of the fatigue load limit (P_u/P). These values are retrieved from four diagrams, while the a_{SKF} is determined by the diagram in Figure 3.22.
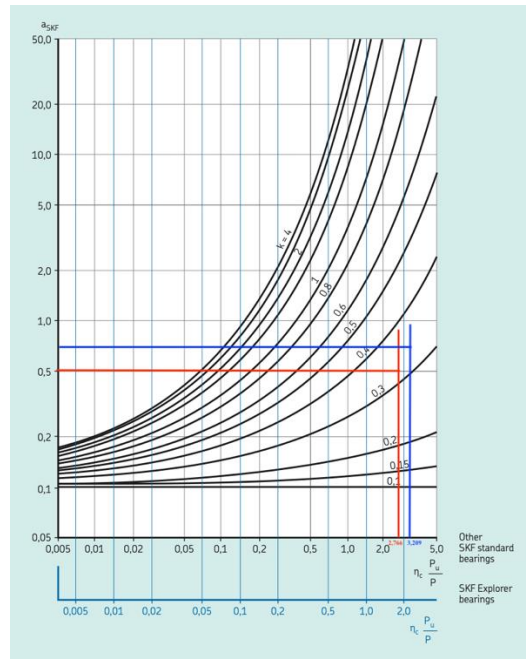
Figure 3.22. Diagram of a_{SKF} values for radial roller bearings (SKF®, 2018). Left bearing is marked in red while the right bearing is marked in blue.

The level of contamination varies depending on the cleanliness conditions of the application. Considering a slight contamination level, then $\eta_c = 0.4$, according to (SKF®, 2018)

The relation of the fatigue load limit is calculated according to the roller bearing properties and equation (3.44):

$$\begin{cases} \left(P_u/P\right)_L = 6.915 \\ \left(P_u/P\right)_R = 8.023 \end{cases}$$

(3.55).

The lubrification condition (κ) is

$$\kappa = \frac{\nu}{\nu_1}$$

(3.56).

where ν is the actual operating viscosity of the lubricant and ν_1 is the rated viscosity. The lubricant chosen is LGMT2 which is an SKF® grease fit for automotive wheel bearings. LGMT2 has a kinematic viscosity of 110 mm^2 s^{-1} at 40 °C (SKF®, 2018). Considering Figure 3.23 and an operating temperature of 70 °C, $\nu = 35$ mm^2 s^{-1}.
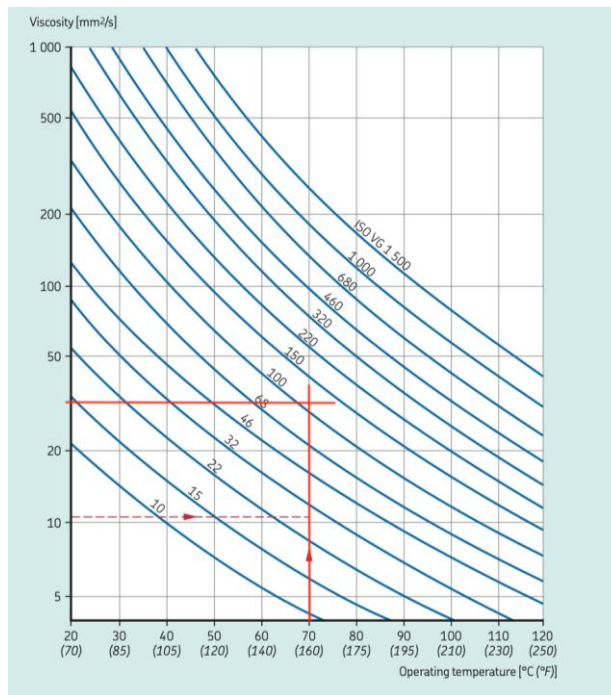
Figure 3.23. Viscosity-temperature diagram for ISO viscosity grades (SKF®, 2018). Grease LGMT2 at 70 ºC marked in red.

Furthermore, the actual operating viscosity depends on the mean diameter of the bearing and its rotational speed, as shown in Figure 3.24. The mean diameter of both bearings is 36 mm for the left bearing and 38.5 mm for the right bearing. Since the rotational speed of the wheel is 16.9 rad s^{-1} or 161.9 rpm then, $\nu_{1L} = 108$ mm^2 s^{-1} and $\nu_{1R} = 128$ mm^2 s^{-1}.
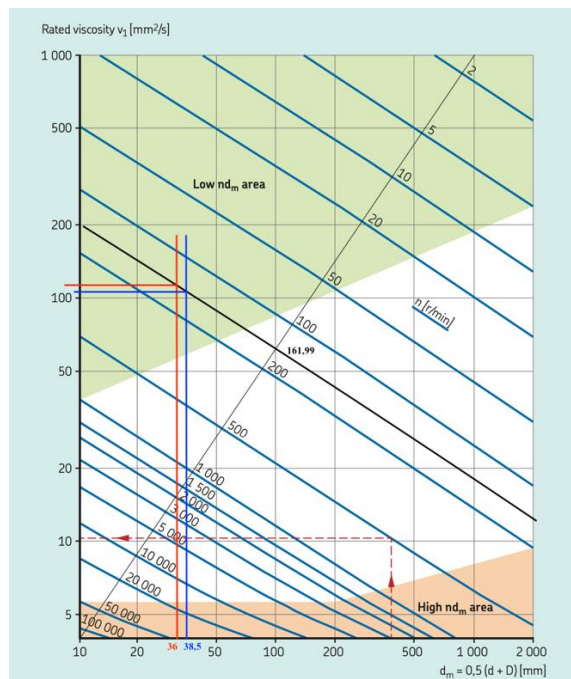
Figure 3.24. Estimated rated viscosity-temperature. Left bearing marked in red and right bearing in blue (SKF®, 2018).

Consequently, using equation (3.56) we can deduce the lubrification condition $\kappa_L = 0.32$ for the left bearing and $\kappa_R = 0.34$ for the right bearing.

The last parameter to be determined is:

$$\begin{cases} \eta_c \cdot \left(P_u/P\right)_L = 2.766 \\ \eta_c \cdot \left(P_u/P\right)_R = 3.209 \end{cases}$$

(3.57).

When analysing Figure 3.22 with equation (3.57) and the lubrification condition values, the a_{SKF} parameter values can be found. Therefore, SKF® life modification factors are 0.5 and 0.75 for the left and right bearing, respectively.

Finally, the SKF® rating life is calculated from equation (3.42):

$$\begin{cases} L_{2mh_L} = 55497196 \text{ h} \\ L_{2mh_R} = 1.1E8 \text{ h} \end{cases}$$

(3.58).

The values obtained in equation (3.58) further validate the bearings with a long SKF® rating life. Hence, these bearings are selected for the suspension knuckle of the AMR.

3.3. Battery and charging

The AMR is going to be used in hospitals and similar environments. Therefore, its layout is complex and has to be flexible to itinerary changes. Also, the robot needs to be as autonomous as possible so it's not feasible to change the batteries manually. After discussing this, we conclude that automatic wireless charging is the optimal choice. Wireless charging allows the robot to charge the dead batteries on the charging station without needing a tight connection between the robot and the charging station. This is due to the fact that this charging method is exempt from the precise positioning of the charger on the charging station. The power transmission is done from the primary coil (on the charging station) to the secondary coil (on the AMR) via electromagnetic induction (Zhang et al., 2013).

The batteries have to be able to attend to the AMRs power needs. It was previously decided that the robot would run on 24 V. Therefore, we need to define how many batteries are needed, their capacity and their autonomy. The number of batteries and their autonomy relies on the battery capacity since

$$B_{Total} = \frac{100 \cdot I \cdot A}{100 - Q}$$ (3.59),

where B_{Total} is the total battery capacity, I is the motor electric current, A is the autonomy and Q is the remaining charge (as in the charge left to power the rest of the AMR except the motor). We can determine the electric current by dividing the voltage (V) by the motor power (P):

$$I = \frac{P}{V}.$$ (3.60)

The number of batteries (n_b) needed are defined in relation to the individual battery capacity (B) available, since:

$$B = \frac{B_{Total}}{n_b}$$ (3.61).

Murata® and Wiferion® are two companies that manufacture lithium-ion batteries. To choose which battery is best suited for the AMR, a spreadsheet was compiled to evaluate the batteries in terms of size, capacity, charging time and charging current. In Figure 3.25 this spreadsheet is shown along with relevant data for the wireless charger.

Battery								
Model	Brand	Capacity [Ah]	Charging Current [A]	Charging time	L x W x H [mm]	Weight [kg]	Communication	Notes
FORTELION Module - Seperate	Murata	24	24	1h	259 x 71 x 245	7,3	CAN Bus	Suitable for low-height AGVs
FORTELION Module - All-In-One		21	42		195 x 132 x 180	6,5	CAN Bus, U-art	-High percise remaining charge calculation -Can be used safely outdoors if need be
etaSTORE LFP	WIFERION		42-420	12min	250 x 190 x 165	-	CANbus	Ideal for continuous use
etaSTORE LTO		22	125 - 150	30min			CANbus	Ideal for high charging currents and many cha

Wireless Charger							
Model	Brand	Charging Power [W]	Charging Current [A]	Optimum distance [mm]	Position tolence	L x W x H [mm]	Communication	Notes
etaLINK 3000	Wiferion	3000	60	15-40	[+/-] 30mm	250 x 15 x 250 OR 150 x 60 x 150	CAN interface	Protection Class: IP68 & IP65
etaLINK 12000		12000	100-600		[+/-] 70mm	320 x 20 x 370		
1 kW Wireless Charger	Delta	1000	max: 41,7	0-20	[+/-] 20mm	Ø 160 x 19	CAN Bus	Protection Class: IP40 & IP65

Figure 3.25. Spreadsheet for the selection process of the batteries and wireless charger. The selected battery and charger are marked in green.

The nominal capacity of the batteries in Figure 3.25 is between 21 and 24 Ah, which means the actual or rated capacity is lower than that. Before sizing the battery, these elements should be considered:

- The remaining charge should be kept at a minimum of 50% to assure there is enough energy to power all of the electronics and lifting mechanism;
- The autonomy should be bigger than three hours to decrease downtime of the AMR.

As previously determined in Sub-section 3.2.3, the motor power is 172 W. However, we are going to use 200 W for safety purposes. So, using equation (3.60) and

equation (3.61), the motor electric current is 8.33 A and the total capacity is 66.67 Ah. This translates to an individual battery capacity of 16.7 Ah, considering 4 batteries. The capacity determined is in line with the nominal capacities shown in Figure 3.25. Thus, four 21 Ah batteries are required for a 50 % remaining charge with 4 h of autonomy.

The 21 Ah batteries in Figure 3.25 have the same size and about the same charging current. The only significant difference is the charging time. The Murata® batteries take one hour to charge while Wiferion® takes only twelve minutes. For this reason, the Wiferion® battery etaSTORE LFP® is chosen.

As for the wireless charger, Wiferion® provides two chargers with different charging power requirements. During the research process, we found another suitable wireless charger manufactured by Delta®. Ultimately, the etaLINK3000® charger was chosen because it is more compact, provides a charging current compatible with the battery chosen and is manufactured by the same company as the battery.

3.4. Control System

Natural feature navigation requires a laser scanner or camera and a PLC. However, these components are not enough to successfully operate the AMR. Brushless DC motors require a controller to keep them running. These motor controllers can also be used for variable speed control (Yedamale, 2003).

When these vehicles are in contact with people, they must be equipped with a safety system. This system is comprised of at least one emergency button and 2 laser scanners. Plus, all electrical components need to comply with a certain safety level. The safety level is measured by two different methods: Performance Level (PL) or Safety Integrity Level (SIL). While SIL measures the integrity level of a component, PL measures the capability of a component to perform a safety task to achieve the expected reduction in risk (SICK®, 2015). The safety levels, PL or SIL, vary according to the ISO 3691-4 standard. The Required Performance Level (PLr) is d. Thus, all electrical components performing safety functions must comply with safety levels of PL d or SIL 2.

The PLC selected for the AMR is the Siemens® SIMATIC S7-1200® series. This programable controller is compact, modular and has already built-in safety functions, so there is no need for an additional safety system. It integrates the safety functions using

PROFINET® or PROFIBUS® via PROFIsafe® (Siemens®, 2017). This PLC is also used by Meng et al. (2019) and Wang et al. (2020) in their projects.

In the case of the AMR, the laser scanner serves two purposes: provide navigation data and monitor the hazardous zone by scanning the area around it. The navigation data is provided to the PLC via port 9000 (for a PROFINET® interface) and the hazardous zone is monitored by two different field ranges: the protective/safety field and the warning field. The protective field is the closest to the AMR and if an object is detected here, the AMR must come to a complete stop. The warning field is a secondary, broader field and if triggered the AMR must decelerate. The laser scanners on the market most suited for the AMR are shown in Figure 3.26.

Laser Scanner								
Model	Brand	Protective Field Range [m]	Warning Field Range [m]	Angle [°]	H x W x D [mm]	Weight [kg]	Communication	Safety	Notes
NANS3-CAAZ30AN1	Sick	3	10	275	106,6x80x117,5	0,67	Ethernet	SIL2, PL d	128 or 8 Fields Power cons.: 3.9 W
SafeZone Mini	Rockwell	2-3	-	270	-	-	-		-
OS32C	Omrom	3-4	10-15		133x104,5x142,7	1,3	Ethernet		Power cons.: 3.75 W
microScan3	Sick	5,5	40	275	112x150,8x111,1	1,45	PROFINET, Ethernet, EtherCAT		120 Fields Power cons.: 7W

Figure 3.26. Laser scanners' properties. The selected one is highlighted in green.

Ultimately the Sick® microScan3® laser is chosen because it has the biggest angle, the biggest warning field range and has a PROFINET® interface even though it is the heaviest, lengthiest and most power-consuming option.

As for emergency buttons, Sick® has the ES21 series. The ES21-SB13J1 is the only complete version that has a panel mount and is illuminable. Thus, this pushbutton is chosen.

To help reduce the risk of failure, the motor controller needs safety functions to be able to stop the motor even if the standard functions are faulty. There are two safety functions for this purpose: Safety Torque Off (STO) and Safe Stop 1 (SS1). The STO assures that the power to the motor is cut and so the motor cannot generate torque. The SS1 initiates the deceleration of the motor and initiates the STO function after a pre-defined time (Grießnig et al., 2010). The latter is not considered crucial and so may not be found in the motor controllers available.

The two motor controller manufactures consulted are Roboteq® and Nanotec®. Both offer controllers compatible with the DB59L024035R-B3 motor and are equipped with the same communication protocols. The key difference between these two brands is safety functions. Roboteq® has a model with certified STO (EN 61800-5-2) while Nanotec® does not have any safety functions certification. For this reason, Nanotec® controllers are discarded as viable options. Roboteq® dual channel motor controllers are shown in Figure

3.27. The dual-channel feature allows for the control of two motors simultaneously, which means that for the AMR only one controller is necessary.

Motor Controller									
Model	Brand	STO	Channels	Max current/channel [A]	L x W x H [mm]	Weight [kg]	Communication	Safety	SSI	Price
FBL2360T		✓		60	140x140x25	0,45	USB, CAN	PLe, SIL3	✓	$745
FBL2360TE		✓					USB, Ethernet, CAN		✓	$825
HBL2360A		☐		75	228x140x25	1,34		-	✓	$745
SBL2360T	Roboteq	✓	2	30	123x83x25	0,22	USB, CAN	PLe, SIL3	✓	$495
SBLM2360T		✓							✓	$575
GBL2660		☐		180	140x200x58	3,00		-	✓	$895
GBL2660E		☐				2,48	USB, CAN, Ethernet	-	✓	$995

Figure 3.27. Roboteq® motor controllers' properties. The final choice is highlighted in bold.

From Figure 3.27, the motor controllers with the STO function and a performance lever over PL d are the FBL, SBL and SBLM series. The maximum current per channel required is 30 A since the peak current of the motor is 28 A (Nanotec®, 2018). Therefore, SBL2360T is chosen because it complies with all the requirements and is cheaper than SBLM2360T.

It is worth noting that the battery charger and motor controller do not have a PROFINET® interface, so the PLC needs to have a gateway module to relay information from one communication protocol to the other.

3.5. Structure

The structure of the AMR can be divided into 3 parts: frame, chassis and lifting mechanism. The frame is the backbone of the AMR while the chassis includes all of the plates and metal sheets that enclose the frame and support other components such as the motors and batteries. The lifting mechanism is a tool to elevate cargo to a certain height.

Firstly, all the components are assembled using the Autodesk Inventor® without the structure. Then the frame skeleton is built on the components assembly so to meet the requirements. The next step is to build the supporting structures for the batteries and motors. The motor support (Figure 3.28) is designed to accommodate the motors side by side and to be bolted to the frame. Moreover, it is made from Aluminium 6061. The two mounting plates have a rectangular protrusion meant to allow the easy removal of the motors. This way the motors can be removed from below without having to disassemble the motor support entirely.
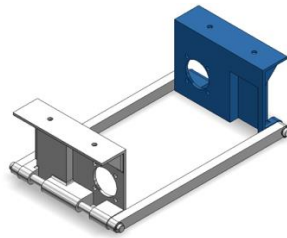
Figure 3.28. Motor support conceptual design.

The battery support is divided into two parts: the fixed part (Figure 3.29A) and the box (Figure 3.29B). The fixed part, as the name implies, is fixed onto the frame while the box is meant to hold two batteries. This two-part support makes it possible for the easy removal of the batteries from the AMR.

(A)   (B)
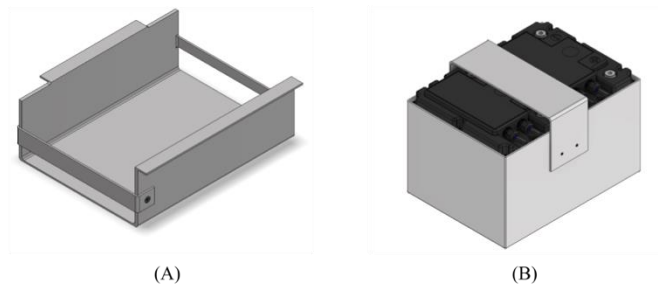
Figure 3.29. Second concept for the battery support: fixed component on the left and battery box on the right.

The fixed part (Figure 3.29A) has a plaque on the front to enable the removal of the battery and it is made from Aluminium 6061, which is bolted to the battery box as well to secure it in place.

The box (Figure 3.29B) has a strap on top, which is bolted to the main box to prevent the batteries from moving up and down while in transit. Both the box and the strap are made from Polypropylene (PP). This material is very light, extremely chemical resistant and almost impervious to water. It is also used for battery boxes, cable insulation, bottles, to name a few applications (Patil et al., 2017).

The laser scanner support (Figure 3.30) is designed next. The laser is secured to the support through a Sick® mounting kit. The support is not only one piece since the top corner is removable to allow direct access to the laser. The support is entirely made from Aluminium 6061.
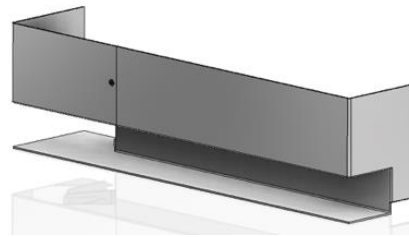
Figure 3.30. Laser support conceptual design.

The suspension system is also connected to the frame to secure it in place. As discussed in Sub-Section 3.2.4, the suspension system is composed of a suspension knuckle and it is secured to the frame by the spring housing as shown in Figure 3.31.
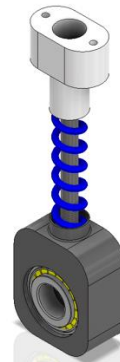
Figure 3.31. Suspension system conceptual design: suspension knuckle is represented in grey and spring housing is represented in white.

The suspension knuckle is represented in dark grey in Figure 3.31 and houses the roller bearings. At the top of the knuckle, a CNS 4320 M12×150 hexagonal bolt secures the spring (in blue in Figure 3.31) to the knuckle and the spring housing (in white in Figure 3.31). The spring housing is fitted with one Igus® iglidur® G sleeve bearing to ease the bolt's movement. The bolt was also assessed using the Design Accelerator® tool. Figure 3.32 shows the strength calculation.
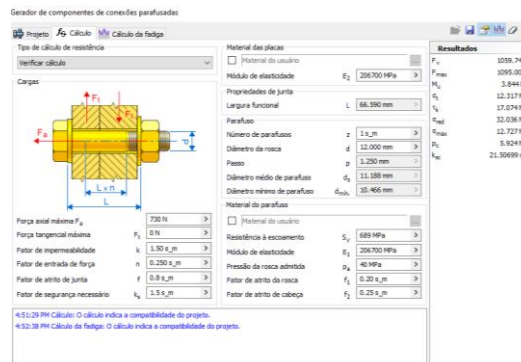
Figure 3.32. Design Accelerator® tool strength calculations for CNS 4320 M12×150 bolt.

An axial force of 730 N is used because it is the maximum force the spring exerts on the spring housing. The joint friction and force input factors using determined by the tool's table of examples. Moreover, a fatigue assessment (Figure 3.33) is also done.
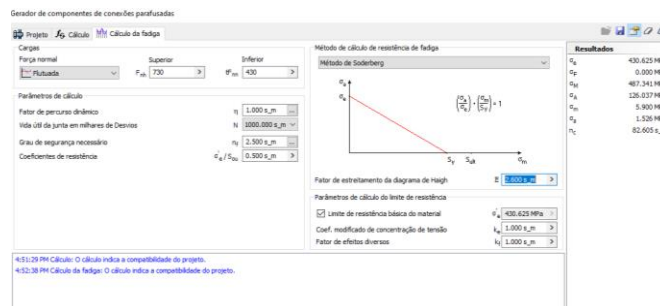
Figure 3.33. Design Accelerator® tool fatigue calculations for CNS 4320 M12×150 bolt.

In the fatigue calculations, a fluctuated load is applied. The inferior and superior values of this load correspond to the pre-load force and maximum force of the spring, respectively.

Before assessing the remaining chassis panels and frame structure, the lifting mechanism is constructed. The AMR is meant to carry loads; therefore, an elevation mechanism is the adequate technology. The initial idea was a type of scissor lift but upon further assessment another concept was drafted. The reason for this is to conserve space and weight since the PLC and respective wiring are positioned among the lifting mechanism.

Andersson & Engström (2018) developed several alternative solutions. One of them, involves an electrical linear actuator. This actuator is connected to a lever and when it is activated it pushes the lever upwards. However, the platform does not elevate vertically. The lever is positioned at an angle and so it has circular motion, which means the platform rises diagonally.

To compensate the circular motion of the lever, a groove is inserted into the long side of the lever. This way the V-profile attachment is able to slide on the lever elevating the platform vertically. This concept only uses two linear actuators. As shown in Figure 3.34, we positioned levers on both sides of the linear actuator. In this layout the actuator is pulling instead of pushing and so pulls both levers simultaneously. Moreover, the linear actuator has to be positioned with enough space to travel up and down, because it is not fixed in any point and moves with the levers.
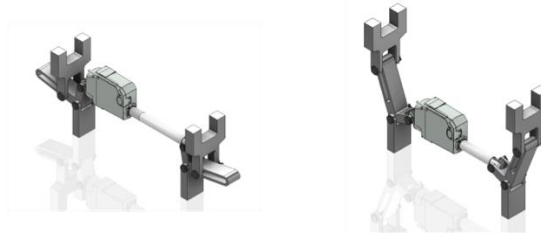
Figure 3.34. Design of the proposed lifting mechanism.

The assessment of the actuator force necessary is done by analysing the free-body diagram of the lever in Figure 3.35.
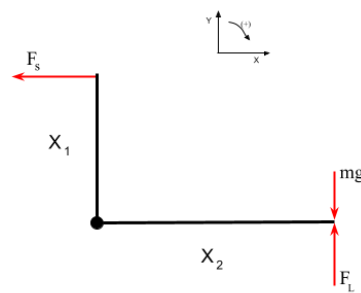
Figure 3.35. Free-body diagram of the lever of the lifting mechanism.

The lever forcer (F_L) has to be bigger than the weight of one-quarter of the load, as the load is distributed over four contact points. Therefore, the lever force must be enough to lift 25 kg (or 245.25 N). Moreover, the actuator force (F_s) is defined by:

$$\text{F}_s = m_q \, g \, \frac{x_2}{x_1}$$

(3.62)

where m_q is the mass of one-quarter of the load, x_1 is the height of the lever and x_2 is the length of the lever. Since the size of the lever is not known and iteration process is done; the lift mechanism needs to be able to lift the platform at least 100 mm. Therefore, according to the actuator force chosen we varied the lever height and calculated the next parameters. The stroke of the platform is retrieved from the design created in Inventor®. This iteration process is shown in Figure 3.36. The only suitable option where the platform stoke is above 100 mm is the last one, marked in green, in Figure 3.36.

Figure 3.36. Iteration process for assessing the size of the lever. The final choice is marked in green.

The linear actuators used in this project are from the same company used by Andersson & Engström (2018), LINAK®. Based on the load requirements, two electric linear actuators are chosen: LA20 and LA23. LA20 has a load pull force of 900 N while LA23 has a pull force load of 1200 N. Length of these actuators' changes depending on the stroke, as shown in Table 3.2.

Table 3.2. LINAK® linear actuators sizes.

Name	Min. width	Stroke	Max. width
LA20	252	70	322
LA23	172	50	222
LA23	222	100	322

In the iteration process we also change the distance between bases since the bigger the distance, the bigger the angle between the base and the lever. This angle should be bigger than zero to avoid the lever to tip forwards but should not be too big to interfere with the actuator's stroke.

To connect the base and lever an ISO 2341 B B -10×60 baltic bolt is used along with a Igus® iglidur® G sleeve bearing to facilitate the rotational movement. Another ISO 2341 B B -10×60 baltic bolt is used to fix the lever to the linear actuator and an ISO 2341 B B -12×70 baltic bolt is selected to connect the lever to the attachment.

The base, lever and attachment are critical parts and so require a Finite Element Analysis (FEA). Because of the complex nature of the lift mechanism the FEA is conducted individually using the Autodesk Inventor® stress analysis add-in. For each part the initial and final position are evaluated. Therefore, two FEA are required per part.

For the base, which is made from Aluminium 6061, the FEA in Figure 3.37 show a maximum stress of 22.23 MPa with a displacement of 0.066 mm for the initial position

and a maximum stress of 10.62 MPa with a displacement of 0.027 mm for the final position. Since Aluminium 6061 has a yield strength of 275 MPa then the base is able to withstand the weight of the load. This analysis is done considering 625731 nodes and 424552 elements, a fixed constraint at the bottom of the base and two loads are applied to the pin holes.
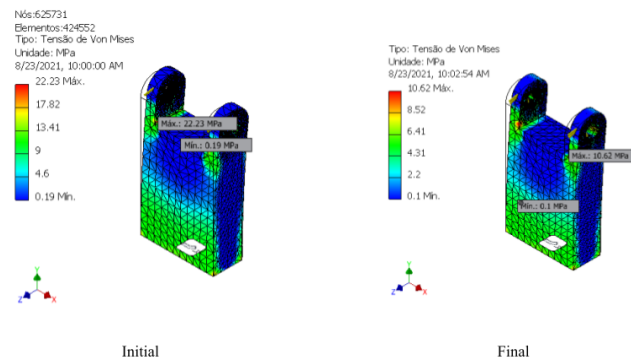
Initial   Final

Figure 3.37. FEA results for the base of the lifting mechanism.

The FEA of the lever results (Figure 3.38) are for the initial position, maximum stress of 19.99 MPa with a displacement of 0.105 mm and for the final position, maximum stress of 10.01 MPa with a displacement of 0.077 mm. The lever is also made from Aluminium and so it is capable of handling the lifting weight.
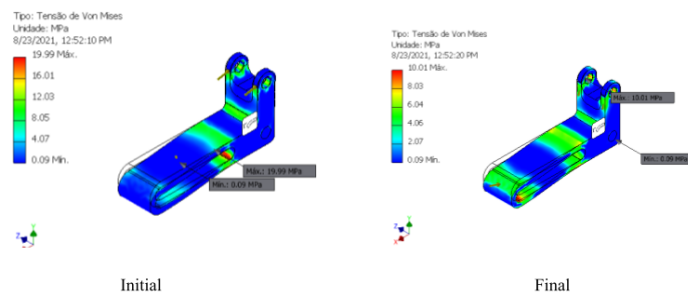
Initial   Final

Figure 3.38. FEA analysis results for the lever of the lifting mechanism.

Finally, the FEA results for the attachment are shown in Figure 3.39. Both in the initial and final position the maximum stress is 1.15 MPa with a displacement of 0.9 μm. Thus, this part, made from Aluminium 6061, can withstand the load weight.

<div align="center">Initial   Final</div>
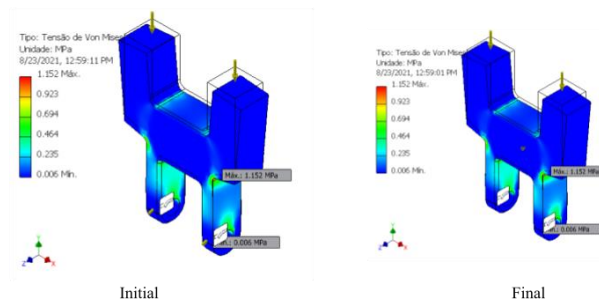
Figure 3.39. FEA analysis results for the attachment of the lifting mechanism.

With all of the components of the lifting mechanism defined, the frame structure and consequently the chassis is finalized. The frame (Figure 3.40) is comprised of two different beams in different sizes: DIN EN 1005 6 leg angle beam and DIN EN 10305-5 rectangular beam.

Figure 3.40 is colour coded so: green is DIN EN 1005 6 L20×20×3, red is DIN EN 1005 6 L25×25×3, yellow is DIN EN 10305-5 30×20×1, blue is DIN EN 10305-5 40×25×1.5 and white is DIN EN 10305-5 60×20×2.
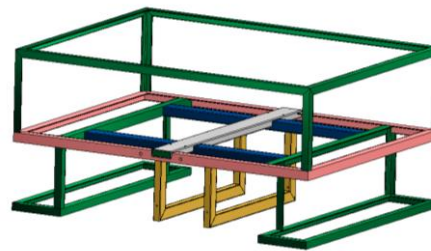
Figure 3.40. Frame concept designed in Inventor®.

Lastly, the remaining panels of the chassis (Figure 3.41) are designed according to the requirements of the AMR. The AMR needs to be completely covered to prevent dirt and dust from coming into contact with components and cause possible damages. Moreover, the access to the components needs to be as simple as possible for maintenance purposes. Furthermore, the battery charger panel must allow good communication between the mobile charger on the AMR and the stationary charger on the charging station.

<div align="center">(A)   (B)</div>
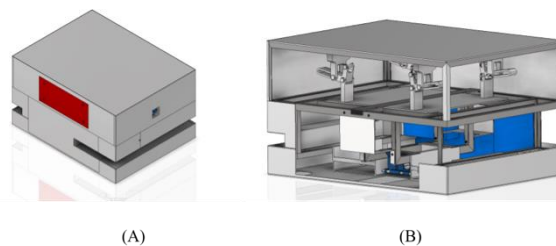
Figure 3.41. AMR chassis designed in Inventor®: A – exterior chassis; B – Interior chassis with frame.

The lower side panels are designed to not interfere with the laser scanners' angle of visibility. The panels are all made from Aluminium 6061 except for the battery charger panel (highlighted in red in Figure 3.41A), the wheel mudguard (highlighted in white in Figure 3.41B) and the panel on top of the AMR (which is made from stainless steel).

The wheel mudguard is fabricated in Acrylonitrile Butadiene Styrene (ABS). This type of material is used in automotive wheel covers and it is a durable thermoplastic (Patil et al., 2017). The battery charger panel needs to be fabricated in plastic as well, since metals interfere with the wireless charging. The battery charging panel is also exposed to the elements, which means that it will be exposed to UV-C lights and cleaning chemicals.

Upon further research on plastics, it proved to be very difficult to find plastics with good UV resistance properties because UV radiation causes photooxidative degradation. This degradation causes the polymer chains to break down and spawn free radicals that reduce the molecular weight and weaken the mechanical properties (Yousif and Haddad, 2013). Moreover, the plastics found with UV resistance are assessed based on the general weathering conditions. Therefore, without a practical test, the plastic selected may need to be replaced after some time in use.

The plastic selected for the battery charger panel is from Ensinger®. The company has developed a conductive plastic with good UV and weather resistance: TECAFORM AH ELS®. This material is an acetal-copolymer fortified with a special conductive carbon. The addition of the carbon gives the material good electrical properties. In addition, this material has excellent chemical resistance and high strength (Ensinger®, 2021).

The bill of materials can be found in APPENDIX B.

4. STRUCTURAL MODELLING

To validate the developed AMR model, its structure has to be analysed. Therefore, stress and modal analysis are conducted as well as a fatigue assessment. The stress analysis is conducted in Autodesk Inventor® and the fatigue assessment and modal analysis are done using COMSOL Multiphysics®. Since the AMR structure is rather complex, the stress analysis conducted in Autodesk Inventor® are verified using COMSOL Multiphysics®.

This chapter is divided into two sub-sections: model definition and results analysis. In the Sub-section 4.1, the model used in all the simulations is presented and Sub-section 4.2 relates to the presentation and discussion of the results.

4.1. Model definition

Before running the Finite Element Analysis (FEA), the model needs to be defined. To further simplify the model and speed up computation time without compromising the validity of the results, only the batteries and traction system weight, payload and the spring force are considered. The values of the forces are presented in Table 4.1 and are obtained based on the suspension spring maximum and minimum forces, the battery, traction and lifting mechanism weight in Autodesk Inventor® and the maximum payload. These values are rounded up for safety.

Table 4.1. Forces applied to the AMR model.

	Value (N)
Max. spring force	730
Min. spring force	470
Battery weight	160
Traction system weight	50
Lift mechanism weight (with load of 100 kg)	1250

The simplified structural model (Figure 4.1) is defined in terms of constraints, loads, contacts, and mesh.
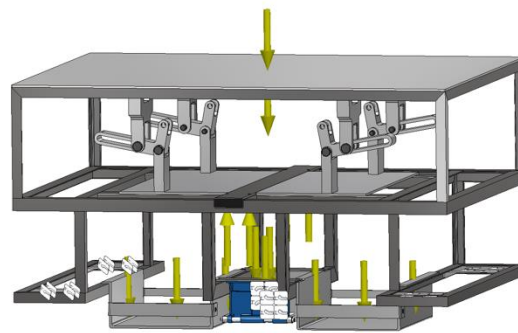
Figure 4.1. Structure model with fixed constraints and appropriate loads (in yellow).

Fixed constraints are positioned on the bolt holes where the gearbox and castors are fixed. The loads applied are the ones presented in Table 4.1 with the exception of the lifting mechanism load. Since the structure is already comprised of the lifting mechanism, only the payload is necessary. Therefore, a load of 1000 N is applied to the top of the AMR. The lifting mechanism is in its initial position because, as seen in Sub-Section 3.5, is the most critical.

Contacts can be done manually or automatically. Because the structure is welded and bolted together, all contacts are done automatically and are assumed as bonded.

Finally, the mesh is defined by adjusting the predefined values. The mesh chosen is finer enough to provide reliable data at a reasonable computational speed.

4.2. Results analysis

Two static analyses are made: one for maximum spring force and another for minimum spring force. The modal analyses are done only once because the forces applied do not interfere with the system's natural frequencies. The fatigue assessment is done considering several loads scenarios.

There is some difference between the results with Autodesk Inventor® and COMSOL Multiphysics®, because of the difference in mesh size and precision of both simulation software. Therefore, this discrepancy is not considered relevant and can be discarded.

4.2.1.   Static Analysis

The goal of the static analysis is to evaluate the model in terms of mass distribution and overall capacity to withstand stresses applied. The mass distribution is

assessed through the constraints' reaction forces on the z-axis. The capacity to bear the stresses applied and to maintain structural integrity is studied through the von Mises stress and the maximum displacement.

It should be noted that, for minimum spring force, the mass being supported by the wheels should not surpass 106 kg. This is because, considering that the AMR's mass is 200 kg with the payload, the springs are lifting 94 kg (47 kg on each side) and therefore the mass on the constraints should be around 106 kg. By the same reasoning, we can find that for maximum spring force the mass supported by the wheels should be around 54 kg.

4.2.1.1. Minimum Spring force

The first results to be analysed are for the case of minimum spring force. The reaction forces from the Autodesk Inventor® and COMSOL Multiphysics® simulations are compared in Table 4.2. The left and right wheel forces in COMSOL Multiphysics® are equal because the simulation results can only show them together.

Table 4.2. Constraints' reaction forces in z the axis for minimum spring force.

Constraint	Autodesk Inventor® F_z (N)	COMSOL Multiphysics® F_z (N)
Left front castor	114.381	110.430
Right front castor	100.888	117.580
Left wheel	266.066	259.305
Right wheel	244.315	259.305
Left back castor	94.6798	114.400
Right back castor	112.784	117.130

To better evaluate the results in Table 4.2, the mass distribution analysis is conducted, as shown in Table 4.3. Since the model is a simplification of the AMR, the mass being supported in the constraints should be below 106 kg, as shown in Table 4.3. Moreover, there is a difference of approximately 2 kg between the left side and right side while the front and back of the AMR is balanced. This discrepancy can be attributed to the fact that the structure is not symmetric.

Table 4.3. Mass distribution for minimum spring force.

	Autodesk Inventor® (kg)	COMSOL Multiphysics® (kg)
Left side	48.43	49.35
Right side	46.69	50.36
Front	21.15	23.60
Middle	52.03	52.87
Back	21.94	23.24
TOTAL (kg)	**95.12**	**99.71**

The maximum displacement values are 0.250 mm and 0.157 mm in COMSOL Multiphysics® and Autodesk Inventor®, respectively, as shown in Figure 4.2. In these simulations two different types of steel materials. Thus, there is a discrepancy of 37 % in maximum displacement values. By analysing Figure 4.2, we can conclude that the most solicitated areas are the same, which means the material has a significant impact on the results.

(A)   (B)
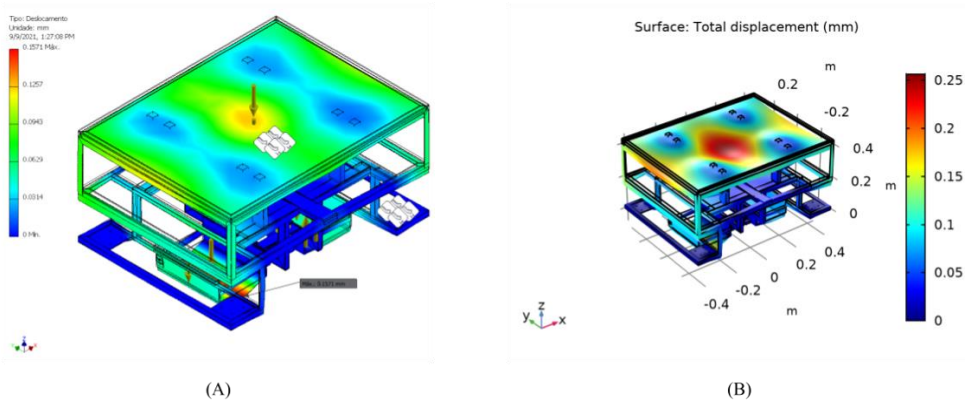
Figure 4.2. Computational results for the total displacement in Autodesk Inventor® (A) and COMSOL Multiphysics® (B) for minimum spring force load case.

The von Mises stress results of the COMSOL Multiphysics® simulation is presented in Figure 4.3. This simulation showed the worst-case scenario and so more worthy of study. The maximum values shown in Figure 4.3 is 1.315 GPa. This value relates to stress concentration points and so is not real. For a better perception of the stresses applied to the structure the range is changed to 5 MPa. The range is set to 5 MPa since the registered average von Mises stress in COMSOL Multiphysics® is about 2 MPa.
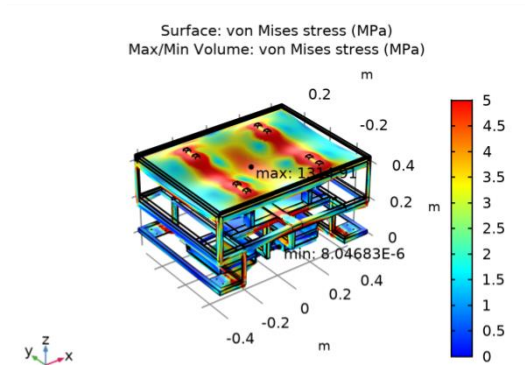
Figure 4.3. Computational results for the COMSOL Multiphysics® for minimum spring force load case.

Given all the information gathered on mass distribution, total displacement, and Von Mises stress we can determine that the AMR is statically approved for when the spring force is at its minimum and it is carrying a load of 100 kg.

4.2.1.2. Maximum Spring force

As for the case of maximum spring force, the results for the reaction forces are presented in Table 4.4. The values have dropped significantly which is logical since the force exerted by the spring has increased.

Table 4.4. Constraints' reaction forces in the z-axis for maximum spring force.

Constraint	Autodesk Inventor® F_z (N)	COMSOL Multiphysics® F_z (N)
Left front castor	95.247	81.250
Right front castor	72.873	91.524
Left wheel	52.501	47.395
Right wheel	33.744	47.395
Left back castor	66.301	81.250
Right back castor	92.245	88.991

The assessment of the mass distribution of this load case is shown in Table 4.5. For this load case there is also a discrepancy between the left and right side of the AMR. Since the difference remains more or less the same in both load cases, the electric components and wiring should be positioned in such a way as to counteract this imbalance.

Table 4.5. Mass distribution for maximum spring force.

	Autodesk Inventor® (kg)	**COMSOL Multiphysics®** (kg)
Left side	21.82	21.40
Right side	20.27	23.23
Front	16.16	17.35
Middle	8.79	9.66
Back	17.14	17.61
TOTAL (kg)	**42.09**	**44.63**

Since these simulations are performed under similar conditions as for the minimum spring force load case, the discrepancies should be identical as well. Therefore, the results are compared to check whether these inconsistencies have compounded in such a way as to invalidate the results.

The von Mises stress simulation results are presented in Figure 4.4. The range has been adjusted for 5 MPa to ignore the stress concentration points. The average von Mises stress should be around 2 MPa as well.
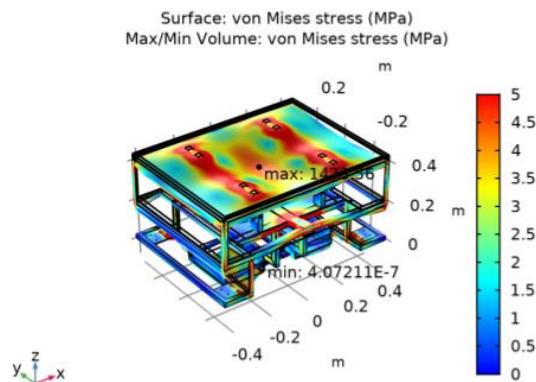
Figure 4.4. Computational results for the Von Mises stress COMSOL Multiphysics® for maximum spring force load case.

The displacement results (Figure 4.5) have maximum values of 0.145 mm and 0.250 mm in Autodesk Inventor® and COMSOL Multiphysics®, respectively. The 39 % disparity are the result the different material properties already discussed for the minimum spring load case.
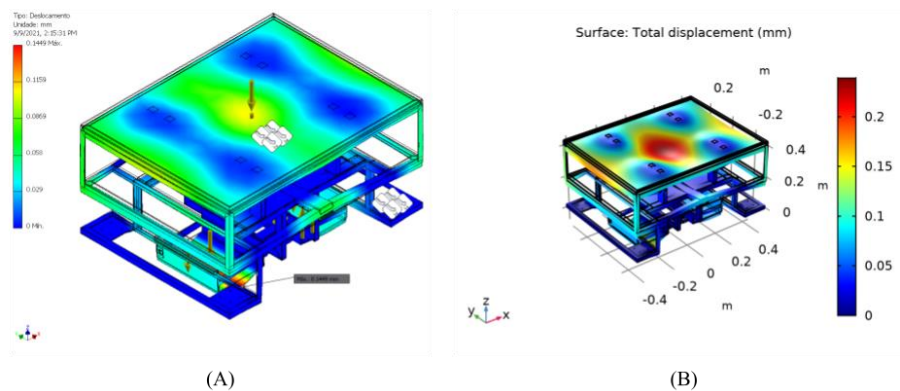
Figure 4.5. Computational results for the total displacement in Autodesk Inventor® (A) and COMSOL Multiphysics® (B) for the maximum spring load case.

As a result, we can conclude that the model is overall subject to low stresses, and it is capable of withstanding the payload required of 100 kg.

4.2.2. Modal Analysis

The natural frequencies of the model should not be close to the natural frequency of the motor to avoid resonance scenarios. Frequency (f) can be expressed in

$$f = \frac{n_m \text{ (rpm)}}{60} \text{ [Hz]}$$

(4.1).

The motor nominal velocity is 2500 rpm, so its natural frequency is 41.7 Hz. Therefore, the simulation is set for 6 frequencies in a range of 40 Hz. The mesh size is the following:

- Maximum and minimum element size: 0.088 and 0.0158;
- Curvature factor: 0.6;
- Resolution of narrow regions: 0.5;
- Maximum element growth rate: 1.45.

The simulation results of the modal analysis are presented Table 4.6.

Table 4.6. Modal analysis simulation results.

Frequencies (Hz)
32.6
34.6
37.1
71.7
89.6
101.1

The first two frequencies in Table 4.6 are very similar and could correspond to degenerate modes. However, after analysing them further we concluded that these two frequencies (32.6 Hz and 34.6 Hz) do not vibrate in the same way and so they identify two independent modes. Furthermore, none of the frequencies shown in Table 4.6 match the natural frequency of the motors. Thus, the risk of a resonance phenomenon occurring due to mode coupling is negligible.

4.2.3. Fatigue Assessment

Since the structure is welded, a fatigue assessment is necessary to determine its life. Firstly, we aimed to do this evaluation by assessing the most critical welding points using the Eurocode 3 standard. However, this proved to be impractical because of the difficulty in determining the stresses acting on the weld throat plane and the actual shape of the weld. Therefore, the fatigue assessment of the model is conducted using the Fatigue Module of COMSOL Multiphysics®. With the stress-life model, it is possible to determine the fatigue life based on the fatigue life curve that relates load cycle stress amplitude to stress (COMSOL Multiphysics®, 2018).

Stress-life models compare the stress amplitude (σ_a)

$$\sigma_a = \frac{\Delta\sigma}{2}$$

<div align="right">(4.2)</div>

to the Wohler curve to predict the number of cycles at that stress amplitude:

$$\sigma_a = k\, f_{SN}(N)$$

<div align="right">(4.3),</div>

where k is a modification factor to account for surface finish, size, reliability, etc. (COMSOL Multiphysics®, 2018).

In a similar exercise, Rodríguez et al. (2017) considered k equal to 0.5 to account for weldments. Therefore, it is decided to use 0.5 and 0.2 as values for k. All of the studies are conducted with a number of cycles cut-off of 10^{20}. If the structure is shown to have a life of 1^{20} cycles it should be considered infinite life.

The first load cycle studied is the payload. In other words, the payload varies from -1000 N to 0 N. The results are presented in Figure 4.6; note that these values are in a $\log_{10}$ scale.
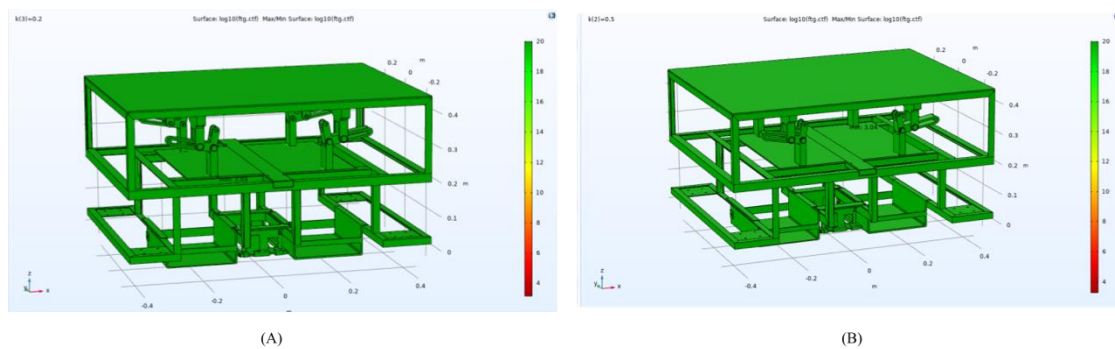
Figure 4.6. Stress-life computational results for k = 0.2 (A) and for k= 0.5 (B) in the payload cycle of -1000 N to 0 N.

Apart from the results obtained in the stress concentrated points, which are to be ignored for reasons already stated, the structure has an infinite life. To further assess the structure the payload cycle is tripled (varies between -3000 N and 0 N) and a new study is conducted, as shown in Figure 4.7.
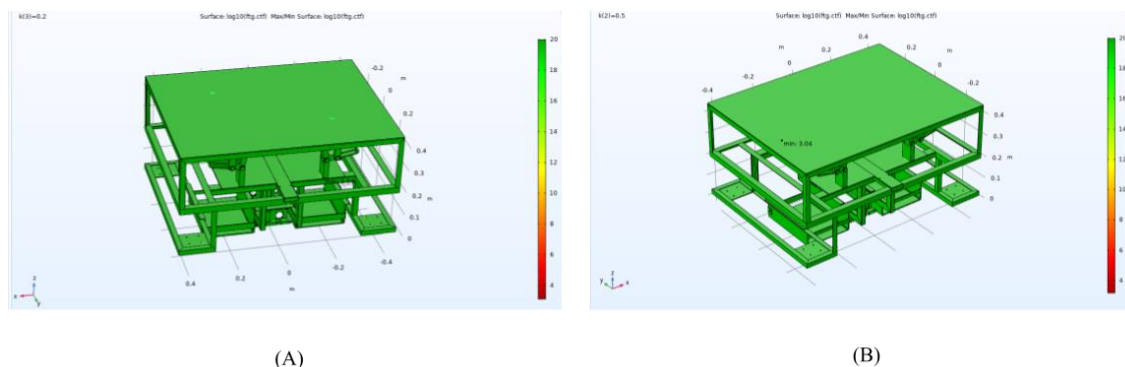
Figure 4.7. Stress-life computational results for k = 0.2 (A) and for k= 0.5 (B) in the payload cycle of -3000 N to 0 N.

Again, the structure is proven to have an infinite life. In a final study (Figure 4.8), another load cycle is imposed: a spring force cycle (700 N to 1000 N) with a payload of 300 kg.

(A)   (B)
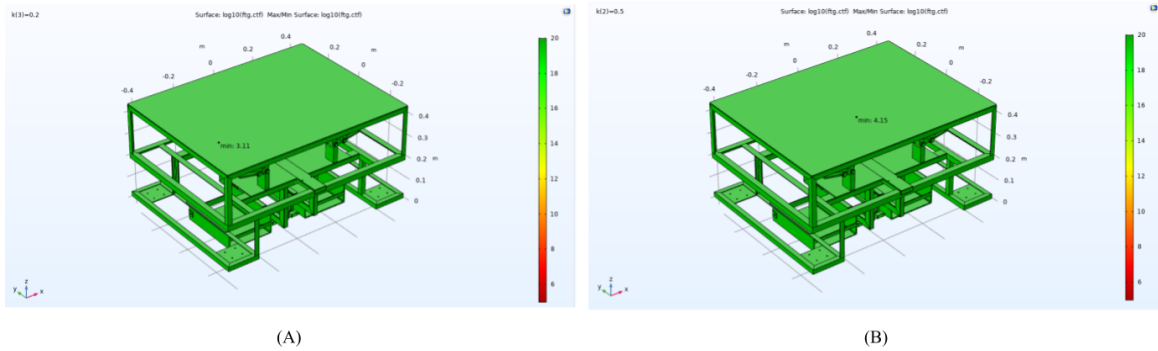
Figure 4.8. Stress-life computational results for k = 0.2 (A) and for k= 0.5 (B) in the spring load cycle of 700 N to 1000 N.

When comparing all of the fatigue studies results, the structure remains with an infinite life despite being subject to loads far superior to the required ones. However, no experimental fatigue tests are conducted to further validate these results. So, we can only conclude that the AMR structure, in theory, can be dynamically approved.

5. CONCLUSIONS AND SUGGESTIONS FOR FUTURE PROJECT

In this dissertation, a concept design of a differential AMR for the healthcare sector is achieved. However, some aspects of the mobile robot such as control system and electronic devices should be extended in subsequent works.

Throughout the design and development stage several companies are contacted for advice on components of the system. Not all contacts have been reciprocated, but the potential suppliers that replied have provided valuable information about specific products and technologies. Also, at this stage several problems appeared that required a solution, being one of these problems the length of the traction unit. Because the motor, gearbox, brake, and encoder system were large, it is not possible to place the engines in line with each other and keep the mobile robot below 70 cm in width. Another problem that was perceived right at the beginning of this study was the material properties of the chassis because they had to be UV-C resistant, and the battery wireless charger could not be covered with metal.

By overcoming most of the problems faced, we are able to design the frame structure and respective chassis. The structure is then subject to static, modal and fatigue analysis to examine its behaviour when specific loads are applied. The static analyses are compared using two different simulation tools, and it is concluded that the AMR should withstand the loads it is subject to without yielding or causing separation of joints. The modal analysis conducted showed that the risk of a resonance phenomenon should not occur. In the fatigue analysis, several load cases are analysed (including cases where the structure is overloaded), which helps solidify the conclusions made with the static and modal analyses.

In conclusion, the modal robot developed in this work is apt to work in the healthcare sector. It is autonomous and because of its suspension system is not vulnerable to floor irregularities unlike other differential robots. It can transport loads up to 100 kg and the lifting mechanism can elevate cargo up to 10 cm. Moreover, it has a simple design and rounded up edges to minimize damages in case of an accident.

5.1. Future work

The mobile robot developed in this dissertation is one of many possible concept designs. To further validate this solution an experimental fatigue test to the critical weldments could be done. Furthermore, the stainless-steel frame designed is not subjected to high stresses and so an aluminium frame could be chosen as an option for the mobile robot. An aluminium frame could also decrease the overall mass of the AMR to below 100 kg.

The designed model has a width of about 690 mm, which even though can pass through 70 cm doors, might have difficulties passing through them at certain angles. To reduce the width, a more compact engine solution should be investigated to decrease the length of the engines and to eliminate the need for a universal telescopic joint.

The material chosen to cover the wireless battery charger, TECAFORM AH ELS®, is only tested for environment level UV light and requires a specific UV-C light test to evaluate its real life.

On a last note, the lifting mechanism is a new concept and therefore could be advantageous to do an experimental test to determine elevation time of different payloads.

BIBLIOGRAPHY

Andersson, R., and F. Engström. 2018. "Compact Lifting Mechanism of Autonomous Vehicle: Concept Development and Guidelines for Implementation."

Archila, J., and M. Becker. 2013. "Mathematical Models and Design of an AGV (Automated Guided Vehicle)." *Proceedings of the 2013 IEEE 8th Conference on Industrial Electronics and Applications, ICIEA 2013* 1857–62. doi: 10.1109/ICIEA.2013.6566670.

Borvorntanajanya, K., P. Thiuthipsakul, S. Chalongwongse, C. Moonjaita, and J. Suthakorn. 2016. "Development of Differential Suspension Wheeled System for Telepresence Robot in Rural Hospital Area." Pp. 1046–51 in *2016 IEEE International Conference on Robotics and Biomimetics (ROBIO)*. IEEE.

Bräunl, T. 2003. *Embedded Robotics*.

Carnegie, D., D. Loughnane, and S. Hurd. 2004. "The Design of a Mobile Autonomous Robot for Indoor Security Applications." *Proceedings of the Institution of Mechanical Engineers, Part B: Journal of Engineering Manufacture* 218(5):533–43. doi: 10.1177/095440540421800507.

Cebollada, S., L. Payá, M. Flores, A. Peidró, and O. Reinoso. 2021. "A State-of-the-Art Review on Mobile Robotics Tasks Using Artificial Intelligence and Visual Data ☆." *Expert Systems With Applications* 167:114195. doi: 10.1016/j.eswa.2020.114195.

Chen, Y., Y. Wu, and H. Xing. 2017. "A Complete Solution for AGV SLAM Integrated with Navigation in Modern Warehouse Environment." Pp. 6418–23 in *2017 Chinese Automation Congress (CAC)*.

Dhaouadi, R., and A. Hatab. 2013. "Dynamic Modelling of Differential-Drive Mobile Robots Using Lagrange and Newton-Euler Methodologies: A Unified Framework." *Advances in Robotics & Automation* 02. doi: 10.4172/2168-9695.1000107.

Dudeja, H., L. Bagal, N. Zunjur, and S. Prof. 2015. "Mechanical Design of an Automated Guided Vehicle (AGV)." *International Journal of Research in Aeronautical and Mechanical Engineering* 3(5):32–40.

Dzezhyts, Y. 2020. *Next Generation Low-Cost Automated Guided Vehicle*. Skovde.

Fragapane, G., R. de Koster, F. Sgarbossa, and J. Strandhagen. 2021. "Planning and Control of Autonomous Mobile Robots for Intralogistics: Literature Review and Research Agenda." *European Journal of Operational Research*. doi: 10.1016/j.ejor.2021.01.019.

Gambhir, Ri., and A. Jha. 2013. "Brushless DC Motor: Construction and Applications." *Int. J. Eng. Sci* 2(5):72–77.

Grießnig, G., R. Mader, C. Steger, and R. Weiß. 2010. "Design and Implementation of Safety Functions on a Novel CPLD-Based Fail-Safe System Architecture." Pp. 206–12 in *2010 17th IEEE International Conference and Workshops on Engineering of Computer Based Systems*.

Hubinský, P., M. Kajan, L. Mrafko, F. Duchoň, and J. Šovčík. 2013. "Control of Automated Guided Vehicle with PLC SIMATIC ET200S CPU." *American Journal of Mechanical Engineering* 1:343–48. doi: 10.12691/ajme-1-7-38.

Lynch, L., T. Newe, J. Clifford, J. Coleman, J. Walsh, and D. Toal. 2018. "Automated Ground Vehicle (AGV) and Sensor Technologies- A Review." Pp. 347–52 in *2018 12th International Conference on Sensing Technology (ICST)*.

Martínez, E. 2020. "Preliminary Design of an Automatic Guided Vehicle(AGV) System." *Undefined* 1–68.

McHaney, R. 1995. "Modelling Battery Constraints in Discrete Event Automated Guided Vehicle Simulations." *International Journal of Production Research* 33(11):3023–40. doi: 10.1080/00207549508904859.

Meena, M., and P. Thilagavathi. 2012. "Automatic Docking System with Recharging and Battery Replacement for Surveillance Robot." *International Journal of Electronics and Computer Science Engineering* 1148–54.

Meng, F., Y. Zhang, and D. Yang. 2019. "Design of Communication Among Vision System, PLC and Industrial Robot Based on Modbus-TCP Protocol." *Journal of Physics: Conference Series* 1288:12083. doi: 10.1088/1742-6596/1288/1/012083.

Parhi, D., and B. Deepak. 2011. "Kinematic Model of Three Wheeled Mobile Robot." *Journal of Mechanical Engineering Research* 3(9):307–18.

Patil, A., A. Patel, and R. Purohit. 2017. "An Overview of Polymeric Materials for Automotive Applications." *Materials Today: Proceedings* 4(2, Part A):3807–15. doi: https://doi.org/10.1016/j.matpr.2017.02.278.

Patricio, R., and A. Mendes. 2020. "Consumption Patterns and the Advent of Automated Guided Vehicles, and the Trends for Automated Guided Vehicles." *Current Robotics Reports* 1(3):145–49. doi: 10.1007/s43154-020-00007-4.

Premi, S. 1985. "The Design of a Free-Ranging Automated Guided Vehicle (AGV) System." Imperial College London.

Razak, M., K. Rasit, N. Nuri, and M. Rashid. 2016. "Structural Design and Analysis of Autonomous Guided Vehicle (AGV) for Parts Supply." *Mechanical Engineering Research Day (MERD)* (March):58–59. doi: 10.13140/RG.2.1.1114.9209.

Reddy, K., M. Kodati, K. Chatra, and S. Bandyopadhyay. 2016. "A Comprehensive Kinematic Analysis of the Double Wishbone and MacPherson Strut Suspension Systems." *Mechanism and Machine Theory* 105:441–70. doi: https://doi.org/10.1016/j.mechmachtheory.2016.06.001.

Rodríguez, A., B. Chiné, and J. Ramírez. 2017. "Fatigue Analysis of an Aluminum Tricycle Frame." in *2017 COMSOL Conference*.

Rubio, F., F. Valero, and C. Llopis-Albert. 2019. "A Review of Mobile Robots: Concepts, Methods, Theoretical Framework, and Applications." *International Journal of Advanced Robotic Systems* 1–22. doi: 10.1177/1729881419839596.

SICK®. 2015. "Guide for Safe Machinery - Six Steps To A Safe Machine."

Singh, S. 2017. "Floor Finish Selection in Hospitaal Design: A Survey of Facility Managers."

Soni, S., T. Mistry, and J. Hanath. 2014. "Experimental Analysis of Mecanum Wheel and Omni Wheel." *International Journal of Innovative Science, Engineering & Technology* 1(3):292–95.

Taipalus, T. 2004. "Using Remote Controlled Service Robot for Fetching Objects in Home Environment."

Tzafestas, S. 2014a. "7 - Mobile Robot Control III: Adaptive and Robust Methods." Pp. 237–68 in, edited by S. G. B. T.-I. to M. R. C. Tzafestas. Oxford: Elsevier.

Tzafestas, S. 2014b. "Mobile Robots." Pp. 1–29 in *Introduction to Mobile Robot Control*. Elsevier.

Ullrich, G. 2015. *Automated Guided Vehicle Systems*. 1st ed. Springer-Verlag Berlin Heidelberg.

Wang, T., R. Dong, R. Zhang, and D. Qin. 2020. "Research on Stability Design of Differential Drive Fork-Type AGV Based on PID Control." *Electronics* 9(7):1072.

Wang, X., and L. Wang. 2021. "A Literature Survey of the Robotic Technologies during the COVID-19 Pandemic." *Journal of Manufacturing Systems*. doi: 10.1016/j.jmsy.2021.02.005.

Xue, X., K. Cheng, and N. Cheung. 2008. "Selection of ELECTRIC MOTOR DRIVES for Electric Vehicles." Pp. 1–6 in *2008 Australasian Universities Power Engineering Conference*. Sydney, NSW, Australia: IEEE.

Yedamale, P. 2003. "Brushless DC (BLDC) Motor Fundamentals." *Microchip Technology Inc* 20(1):3–15.

Yousif, E., and R. Haddad. 2013. "Photodegradation and Photostabilization of Polymers, Especially Polystyrene: Review." *SpringerPlus* 2:398. doi: 10.1186/2193-1801-2-398.

Zhang, J., G. Song, Y. Li, G. Qiao, and Z. Li. 2013. "Battery Swapping and Wireless Charging for a Home Robot System with Remote Human Assistance." *IEEE Transactions on Consumer Electronics* 59(4):747–55. doi: 10.1109/TCE.2013.6689685.

WEBOGRAPHY

Active Space Technologies. 2020. "ActiveONE." Retrieved June 22, 2021 (https://www.activespaceautomation.com/agv/activeone/).

Association for Advancing Automation. 2021. "AGV Navigation: What Are the Possibilities?" Retrieved June 8, 2021 (https://www.automate.org/news/agv-navigation-what-are-the-possibilities).

Blickle®. 2020. "Blickle G16 General Catalogue." 1–636. Retrieved April 8, 2021 (http://catalogue.blickle.com).

Caetano, M. 2019. "Propriedades Tribológicas." Retrieved July 2, 2021 (https://www.ctborracha.com/borracha-sintese-historica/propriedades-das-borrachas-vulcanizadas/propriedades-tribologicas/).

Centers for Disease Control and Prevention. 2016. "Disinfection." *Guideline for Disinfection and Sterilization in Healthcare Facilities (2008)*. Retrieved May 26, 2021 (https://www.cdc.gov/infectioncontrol/guidelines/disinfection/disinfection-methods/index.html).

Chen, Y., Y. Wu, and H. Xing. 2017. "A Complete Solution for AGV SLAM Integrated with Navigation in Modern Warehouse Environment." Pp. 6418–23 in *2017 Chinese Automation Congress (CAC)*.

COMSOL Multiphysics®. 2018. "Fatigue Module User's Guide Version 5.4." Retrieved September 1, 2021 (Fatigue Module User's Guide version 5.4).

Ensinger®. 2021. "TECAFORM AH ELS Black." Retrieved July 6, 2021 (https://www.ensingerplastics.com/en/shapes/products/conductive-esd-acetal-tecaform-ah-els).

FDA. 2021. "UV Lights and Lamps: Ultraviolet-C Radiation, Disinfection, and Coronavirus." Retrieved June 27, 2021 (https://www.fda.gov/medical-devices/coronavirus-covid-19-and-medical-devices/uv-lights-and-lamps-ultraviolet-c-radiation-disinfection-and-coronavirus).

Fibro®. 2021. "Fibro - Standard Parts." 1–1350. Retrieved July 1, 2021 (https://www.fibro.de/fileadmin/FIBRO/Blaetterkataloge/NormalienGesamtkatalog_EN/HTML5/).

Mobile Industrial Robots A/S®. 2020. "MiR500." Retrieved March 10, 2021 (https://www.mobile-industrial-robots.com/en/solutions/robots/mir500/).

Nanotec. 2018. "Product Catalog 2018/2019." Retrieved April 16, 2021 (https://en.nanotec.com/fileadmin/files/Katalog/nanotec_catalog_2019.pdf).

Omron®. 2021. "LD Series Autonomous Mobile Robots." Retrieved March 3, 2021 (https://automation.omron.com/en/us/products/family/LD).

OZ ROBOTICS®. 2021a. "Aluminum Mecanum Wheel Basic Right." Retrieved May 27, 2021 (https://ozrobotics.com/shop/5-inch127mm-aluminum-mecanum-wheel-basic-right-14198r/).

OZ ROBOTICS®. 2021b. "Aluminum Omni Wheel with Bearing Rollers and Keyway ." Retrieved May 27, 2021 (https://ozrobotics.com/shop/127mm-heavy-duty-aluminum-omni-wheel-with-bearing-rollers-and-keyway/).

Roboteq®. 2018. "How SSI Encoders Work." Retrieved April 6, 2021 (https://www.roboteq.com/applications/all-blogs/15-how-ssi-encoders-work).

SICK®. 2015. "Guide for Safe Machinery - Six Steps To A Safe Machine."

Siemens®. 2017. "SIMATIC Safety Integrated – All Built In." 1–12. Retrieved May 13, 2021 (https://assets.new.siemens.com/siemens/assets/api/uuid:5d22a993-e055-4e88-a1ff-1ab66a3f3f05/3-63982-version-von-dffa-b10151-02-ws-simatic-safety-1-dffa-b101.pdf).

SKF®. 2018. "Rolling Bearings." 1–1143. Retrieved July 6, 2021 (https://www.skf.com/binaries/pub12/Images/0901d196802809de-Rolling-bearings---17000_1-EN_tcm_12-121486.pdf).

UBTECH®. 2020. "ADIBOT Brochure." Retrieved March 10, 2021 (https://cdn.shopify.com/s/files/1/2265/4045/files/ADIBOT_BROCHURE_2020.pdf?v=1606332802).

World Health Organisation. 2021. "WHO Coronavirus (COVID-19) Dashboard." Retrieved September 21, 2021 (https://covid19.who.int).

ANNEX A

Figure 0.1. Safety factor table (Blickle® 2020).

Legend:
+ resistant
0 resistant under certain conditions
x not resistant
L pitting, stress cracks
- no information

	Concentration in %	Rubber	TPE	Nylon	Polypropylene (PP Copo)	Polyurethane (ester) TPU / Extrathane / Softhane / Vulkollan	Polyurethane (ether) Besthane / Besthane Soft	Stainless steel (V2A, 1.4301, AISI 304)
1-Propanol		+	0	+	+	0	0	+
Acetaldehyde	40	0	+	0	+	0	+	0(L)
Acetic acid (ethanoic acid)	30	x	0	x	x	x	x	+
Acetone		+	0	+	+	0	x	+
Acrylic acid > 30 °C		-	+	x	+	x	x	-
Alkyl alcohol		+	+	0	+	0	0	+
Alkylbenzenes		x	0	+	0	-	-	+
Aluminum acetate, aqueous		+	+	+	+	x	0	+
Amines, aliphatic		0	0	+	+	x	x	+
Ammonia, aqueous	20	+	+	+	+	x	x	+
Ammonium carbonate, aqueous		+	+	-	+	x	x	+
Ammonium chloride		+	+	-	+	x	x	0(L)
Ammonium hydroxide, aqueous	10	-	+	+	+	x	x	+
Ammonium nitrate, aqueous		0	+	+	+	0	+	+
Ammonium salts		-	-	-	+	-	-	-
Ammonium sulfate, aqueous		0	+	+	+	+	+	+
Amyl acetate, aqueous		0	+	+	0	x	x	+
Aniline (aminobenzene)		x	0	0	+	x	x	+
Beer		+	+	+	+	+	+	+
Benzine		x	x	+	0	+	+	+
Benzol		x	x	+	x	x	x	+
Bitumen		x	0	+	+	+	+	+
Bleaching lye (sodium hypochlorite)	10	x	+	x	0	x	0	0(L)
Borax (sodium tetraborate)		+	+	+	+	+	+	+
Boric acid, aqueous	10	+	+	0	+	0	+	+
Bromine		x	0	x	x	x	x	x
Butter		x	+	+	+	+	+	+
Calcium salts, aqueous		+	+	x	+	0	0	+
Carbolineum		x	-	+	+	x	x	-
Carbon monoxide, dry		0	+	+	0	x	x	+
Carbon tetrachloride		x	x	+	x	x	x	+
Castor oil		+	+	+	+	+	+	+
Caustic potash, aqueous (potassium hydroxide)		0	+	+	+	0	+	+
Caustic soda (sodium hydroxide)		+	+	+	+	x	x	+
Chlorine, hydrogen chloride		x	0	x	x	x	x	x
Chromic acid, aqueous	10	x	0	0	+	x	0	+
Citric acid, aqueous	10	+	+	+	+	+	+	+
Copper chloride, aqueous		+	+	0	+	0	+	x
Copper salts, aqueous	10	+	+	x	+	0	+	-
Cottonseed oil		x	x	+	+	+	+	+
Cresols		x	x	x	0	x	x	+
Crude oil		x	x	+	+	+	+	+
Cyclohexanol (Hexalin, Anol)		0	0	+	0	0	x	+
Cyclohexanone		0	0	+	0	0	x	+
Descaler, aqueous	10	-	-	+	+	0	+	+
Detergent solution, 80°C		+	+	+	0	x	0	+
Dichlorobenzene		x	x	+	0	x	x	+
Dichloroethene		x	0	-	-	x	x	-
Diethylene glycol		+	+	0	+	0	0	+
Dimethyl ether		0	0	+	x	x	x	+
Dimethylaniline		x	0	0	x	x	x	+
Dimethylformamide		0	+	+	+	x	0	+
Ethanol		+	0	0	+	+	+	+
Ether (Diethylether)		x	0	+	x	+	+	+
Ethyl acetate (acidic ether)		0	0	+	0	x	x	0
Ethylene (ethene)		x	+	0	+	+	+	x
Fatty acids (oleic acids)		x	0	+	+	0	+	+
Flue gas		0	-	-	-	x	x	+
Formaldehyde (methanal)	30	+	+	+	+	0	0	+
Formamide, pure (methanamide)		+	0	+	+	x	x	+
Formic acid	10	0	+	x	+	x	x	+
Furfural (furfurol)		x	x	0	x	x	x	+

	Concentration in %	Rubber	TPE	Nylon	Polypropylene (PP Copo)	Polyurethane (ester) TPU / Extrathane / Softhane / Vulkollan	Polyurethane (ether) Besthane / Besthane Soft	Stainless steel (V2A, 1.4301, AISI 304)
Glycol (ethylene glycol)		+	+	0	+	0	0	+
Hexan		x	0	+	0	+	+	+
Hydraulic fluid		x	x	+	0	x	x	+
Hydrochloric acid, aqueous	30	0	+	x	+	x	0	x
Iodine tincture		+	+	x	+	x	x	0(L)
Iron chloride, aqueous	10	0	+	x	+	0	+	x
Iron sulfate (iron vitriol)	10	+	+	0	+	0	+	+
Isopropyl chloride		x	0	+	0	x	x	-
Isopropyl ether (diisopropyl ether)		0	0	x	+	+	+	+
Lactic acid		x	+	x	+	x	x	0
Magnesium salts, aqueous	10	+	+	+	+	0	+	0(L)
Malic acid		0	+	+	+	x	0	+
Mercury chloride, aqueous		+	+	x	+	+	+	0(L)
Methyl alcohol (methanol)		0	+	0	+	+	0	+
Methyl ethyl ketone (butanone)		x	0	+	0	x	x	+
Methylene chloride (dichloromethane)		x	x	x	x	x	x	+
Milk		+	+	+	+	0	+	+
Mineral oils		x	x	+	0	+	+	+
Monobromobenzene (bromobenzene)		x	x	0	+	x	x	+
Mortar, cement, chalk		+	+	+	+	+	0	+
Mustard		-	-	+	+	+	+	0(L)
Naphthalene (mineral naphtha)		x	0	+	0	0	0	+
Nickel chloride, aqueous	10	+	+	0	+	0	+	0(L)
Nickel sulfate, aqueous	10	0	+	0	+	0	+	+
Oleic acid (oleinic acid, fatty acid)		x	0	+	+	0	+	+
Oxalic acid, aqueous	10	0	+	0	+	x	x	0
Ozone, atmospheric concentration		x	0	x	0	+	+	-
Palmitic acid (hexadecanoic acid)		x	0	+	0	0	+	+
Phenylbenzene (biphenyl, dibenzol)		x	x	-	-	x	x	+
Phosphoric acid, aqueous	10	0	+	x	+	0	+	+
Plant oils		x	x	+	0	+	+	+
Potassium chloride, aqueous (sylvin)	10	0	+	x	+	+	+	+
Potassium hydroxide, aqueous (caustic potash, potash lye)		0	+	+	+	0	+	+
Potassium sulfate		+	+	+	+	+	+	+
Propane		x	0	+	+	+	+	+
Road salt (solutions)		+	+	+	+	0	+	0(L)
Skydrol		x	x	+	+	x	x	+
Sodium carbonate, aqueous (soda)	10	+	+	+	+	x	x	+
Sodium chloride, aqueous (table salt)	10	0	+	+	+	0	+	0(L)
Sodium hydroxide, aqueous (caustic soda)	10	+	+	+	+	x	x	+
Sodium phosphate, aqueous	10	+	+	+	+	+	+	+
Sodium silicate, aqueous	10	+	+	+	+	x	0	+
Sodium sulfate, aqueous (Glauber salt)	10	0	+	+	+	0	+	+
Sodium sulfide, aqueous	10	0	+	+	+	0	0	+
Sodium thiosulfate, aqueous (antichlor)	10	0	+	+	+	0	+	0(L)
Stearic acid, aqueous		x	+	+	0	x	+	+
Sulfuric acid		0	+	x	+	x	x	+
Tannic acid	10	+	+	+	+	0	+	+
Tartaric acid, aqueous	10	+	+	0	+	0	+	+
Toluene (methylbenzene)		x	x	+	x	x	x	+
Trichloroethylene		x	x	0	0	x	x	+
Turpentine		x	x	+	x	x	x	+
Uric acid, aqueous	10	0	+	+	+	0	-	0(L)
Urine		+	+	+	+	0	+	0(L)
Vaseline		x	0	+	0	+	+	+
Wastewater		-	+	+	+	0	0	-
Water (seawater)		+	+	+	+	0	0	0(L)
Water up to 80°C		0	+	+	0	x	x	+
Water, cold		+	+	+	+	+	+	+
Xylene		x	x	+	x	x	x	+
Zinc chloride, aqueous	10	+	+	0	+	x	x	x

Figure 0.2. Resistance of tread materials to chemicals (Blickle® 2020).

APPENDIX A

Table 0.1. List of chemical disinfectants used in hospitals. This list is a combination of data from AST and Centers for Disease Control and Prevention (2016).

Chemical	Description
Quaternary ammonium compounds	-Environmental sanitization of noncritical surfaces: floors, walls and furniture. -Appropriate to disinfect medical equipment that contacts intact skin.
Phenolic compounds	- Environmental sanitization of surfaces: bedrails, bedside tables and laboratory surfaces. -Noncritical medical devices
Peracetic Acid	- Sterilize medical, surgical and dental instruments (expect dental handpieces).
Iodophors	-Used as an antiseptic. -Disinfecting blood culture bottles and medical equipment.
Hydrogen Peroxide	-Commercially available hydrogen peroxide is used to clean inanimate surfaces. -Higher concentrations can be used to disinfect contact lenses, tonometer biprisms, ventilators, fabrics and endoscopes.
Glutaraldehyde	- High-level disinfectant for medical equipment: endoscopes, dialyzers, transducers, anaesthesia and respiratory therapy equipment, to name a few. -Should not be used to clean noncritical surfaces since it is too toxic and expensive.
Formaldehyde	-High-level disinfectants and their uses are limited because of their irritating fumes and pungent odour. -Can be used to disinfect dialysis machines or to sterilize surgical instruments (when mixed with ethanol).
Ortho-phthalaldehyde (OPA)	-High-level disinfectant with the same uses as glutaraldehyde.
Sodium hypochlorite	- Most commonly known as bleach. -Low-level disinfectant for noncritical environmental surfaces.

APPENDIX B

Part Name	Description	Quantity
DIN EN 10056-1 L20×20×3	DIN EN 10056	20
DIN EN 10056-1 L25×25×3		6
DIN EN 10305-5 L60×20×2	DIN EN 10305	1
DIN EN 10305-5 L40×25×1.5		2
DIN EN 10305-5 L30×20×1		6
TRCT_01	Motor fix; custom made; Aluminium 6061	1
TRCT_02	Motor fix inverted; custom made	
TRCT_03	Fixture truss; custom made	2
TRCT_04	8×148,8 mm axle; Stainless steel	
DIN 471 8×0.8	DIN 471	4
DB59L024035R-B3	Nanotec® BLDC motor	2
BRAKE-BWA-1.5-6.35	Nanotec® motor brake	
NME2-SSI-V06-12-C	Nanotec® motor encoder	
GP56-S2-16-SR	Nanotec® gearbox	
23412-120260	Norelem® telescopic universal joint; machined	
DIN 6885-1 A 4×4-16	DIN 6885-1 A	4
GSTN-127 25H7	Blickle® traction wheel; machined	2
TRCT_05	Wheel axle; 115.7 mm length; Stainless steel	
DIN EN ISO 703-2×12	DIN EN ISO 703	

DIN 9021×26	DIN 9021	
ISO 4017 M12×30	ISO 4017	
TRCT_06	Castor wheel support; custom made; Aluminum 6061	4
LPA-TPA 75G-ELS	Blickle® castor wheel	
DIN ISO 7045H M5×12	DIN ISO 7045H	16
DIN 125-1 A×5.3	DIN 125-1 A	24
DIN EN ISO 10511 M5	DIN EN ISO 10511	20
TRCT_07	Motor fix support; custom made; Stainless steel 316	2
DIN 7985(Z) M5×14	DIN 7985(Z)	4
SUS_01	Suspension knuckle; custom made; Aluminum 6061	2
32005 X	SKF® 32005 X tapered roller bearing	
30205	SKF® 30205 tapered roller bearing	
CNS 4320×150	CNS 4320	
DIN EN 24017 M4×16	DIN EN 24017	8
DIN 125-1 A×4.3	DIN 125-1 A	
GSM-1214-12	Igus® plain bearing	2
241.15.127	Fibro® high performance compression spring: Blue DIN ISO 1043	
SUS_02	Spring housing upper plate	
DIN ISO 4762 M5×50	DIN ISO 4762	4
BTRY_01	Charger chassis panel; custom made; Aluminum 6061	1
BTRY_02	Charger panel; custom made; TECAFORM AH ELS®	
DIN EN ISO 10642 M8×40	DIN EN ISO 10642	4
DIN EN ISO 2009 M2×3	DIN EN ISO 2009	

DIN EN ISO 10511 M8	DIN EN ISO 10511	
DIN 125-1 A×8.4	DIN 125-1 A	
Mobile coil	Wiferion® etaLINK 3000® mobile coil	1
Coil cable	Wiferion® etaLINK 3000® coil cable	
Battery Controller	Wiferion® etaLINK 3000® mobile eletronics	
BTRY_03	Battery support; custom made; Aluminum 6061	
BTRY_04		
BTRY_05	Battery secure bar; custom made; Aluminum 6061	2
DIN ISO 7046 H M4×5	DIN ISO 7046 H	4
BTRY_06_01	Battery box; custom made; Polypropylene	2
BRTY_06_02	Battery lid; custom made; Polypropylene	
DIN ISO 7046 H M2×4	DIN ISO 7046 H	8
Battery	Wiferion® etaSTORE 3000® LFP	4
ES21-SB12J1	SICK® emergency button	1
MICS3-SSAZ55PZ1P01	SICK® Laser scanner; Profinet	2
PLC	Siemens® S7-1200	1
SBL2360T	Roboteq® motor controller	
ELV_01	Lift base; custom made; Aluminum 6061	4
ELV_02	Lift L link; custom made; Aluminum 6061	
ELV_03	Lift load support; custom made; Aluminum 6061	
ISO 2341B-10×6	ISO 231B	
ISO 2341B-12×70		
DIN EN 22341 B B-10×45	DIN EN 22341 B B	

DIN EN 1234 3.2×20	DIN EN 1234	12
LA23	Linak® LA23 linear actuator	2
GSM-101-30	Igus® plain bearing	4
ELV_04	Lift support base; custom made; stainless steel 316	1
PNL_01	Bottom panel; custom made; Aluminum 6061	
PNL_02	Laser scanner; custom made; Aluminum 6061	2
PNL_03	Laser access panel; custom made; Aluminum 6061	
PNL_04	Emergency stop panel; custom made; Aluminum 6061	1
PNL_05	Wheel mudguard; custom made; ABS plastic	2
PNL_06	Battery door; custom made; Aluminum 6061	
PNL_07	Battery door; custom made; Aluminum 6061	
PNL_08	Lower side panel; custom made; Aluminum 6061	1
PNL_09	Upper back panel; custom made; Aluminum 6061	
PNL_10	Upper side panel; custom made; Aluminum 6061	
PNL_11	Top panel; custom made; Stainless steel 316	
DIN ISO 10642 M4×8	DIN ISO 10642	2
DIN ISO 10642 M5×12	DIN ISO 10642	
DIN EN ISO 4036 M5	DIN EN ISO 4036	4
DIN 6797 J×5.3	DIN 6797 J	